The Astrophysical Journal Supplement Series, 224:33 (19pp), 2016 June doi:10.3847/0067-0049/224/2/33

CLASH-VLT: DISSECTING THE FRONTIER FIELDS GALAXY CLUSTER MACS J0416.1-2403 WITH ∼800 SPECTRA OF MEMBER GALAXIES

I. Balestra[1,2], A. Mercurio[3], B. Sartoris[1,4], M. Girardi[1,4], C. Grillo[5], M. Nonino[1], P. Rosati[6], A. Biviano[1], S. Ettori[7,8], W. Forman[9], C. Jones[9], A. Koekemoer[10], E. Medezinski[11,12], J. Merten[13], G. A. Ogrean[9,14,25], P. Tozzi[15], K. Umetsu[16], E. Vanzella[7], R. J. van Weeren[9], A. Zitrin[11,25], M. Annunziatella[1,4], G. B. Caminha[6], T. Broadhurst[17], D. Coe[10], M. Donahue[18], A. Fritz[19], B. Frye[20], D. Kelson[21], M. Lombardi[22], C. Maier[23], M. Meneghetti[7,8], A. Monna[2], M. Postman[10], M. Scodeggio[19], S. Seitz[2,24], and B. Ziegler[23]

[1] INAF—Osservatorio Astronomico di Trieste, via G. B. Tiepolo 11, I-34131, Trieste, Italy; balestra@oats.inaf.it
[2] University Observatory Munich, Scheinerstrasse 1, D-81679 München, Germany
[3] INAF—Osservatorio Astronomico di Capodimonte, Via Moiariello 16, I-80131 Napoli, Italy
[4] Dipartimento di Fisica, Università degli Studi di Trieste, Via Tiepolo 11, I-34143, Trieste, Italy
[5] Dark Cosmology Centre, Niels Bohr Institute, University of Copenhagen, Juliane Maries Vej 30, DK-2100 Copenhagen, Denmark
[6] Dipartimento di Fisica e Scienze della Terra, Università di Ferrara, Via Saragat 1, I-44122, Ferrara, Italy
[7] INAF—Osservatorio Astronomico di Bologna, Via Ranzani 1, I-40127 Bologna, Italy
[8] INFN—Bologna, Via Ranzani 1, I-40127, Bologna, Italy
[9] Harvard-Smithsonian Center for Astrophysics, 60 Garden Street, Cambridge, MA 02138, USA
[10] Space Telescope Science Institute, 3700 San Martin Drive, Baltimore, MD 21208, USA
[11] Cahill Center for Astronomy and Astrophysics, California Institute of Technology, MS 249-17, Pasadena, CA 91125, USA
[12] Center for Astrophysics and Planetary Science, Racah Institute of Physics, The Hebrew University, Jerusalem 91904, Israel
[13] Department of Physics, University of Oxford, Keble Road, Oxford OX1 3RH, UK
[14] KIPAC, Stanford University, 452 Lomita Mall, Stanford, CA 94305, USA
[15] INAF—Osservatorio Astrofisico di Arcetri, Largo E. Fermi 5, I-50125, Firenze, Italy
[16] Institute of Astronomy and Astrophysics, Academia Sinica, P.O. Box 23-141, Taipei 10617, Taiwan
[17] Ikerbasque, Basque Foundation for Science, Alameda Urquijo, 36-5 Plaza Bizkaia, E-48011, Bilbao, Spain
[18] Department of Physics and Astronomy, Michigan State University, East Lansing, MI 48824, USA
[19] INAF—Istituto di Astrofisica Spaziale e Fisica cosmica (IASF) Milano, via Bassini 15, I-20133 Milano, Italy
[20] Department of Astronomy/Steward Observatory, University of Arizona, 933 North Cherry Avenue, Tucson, AZ 85721, USA
[21] Observatories of the Carnegie Institution of Washington, Pasadena, CA 91101, USA
[22] Dipartimento di Fisica, Università degli Studi di Milano, via Celoria 16, I-20133, Milan, Italy
[23] University of Vienna, Department of Astrophysics, Türkenschanzstrasse 17, A-1180, Wien, Austria
[24] Max-Planck-Institut für extraterrestrische Physik, Postfach 1312, Giessenbachstrasse, D-85741, Garching, Germany
Received 2015 November 8; accepted 2016 March 3; published 2016 June 8

ABSTRACT

We present VIMOS-Very Large Telescope (VLT) spectroscopy of the Frontier Fields cluster MACS J0416.1-2403 ($z = 0.397$). Taken as part of the CLASH-VLT survey, the large spectroscopic campaign provided more than 4000 reliable redshifts over ∼600 arcmin^2, including ∼800 cluster member galaxies. The unprecedented sample of cluster members at this redshift allows us to perform a highly detailed dynamical and structural analysis of the cluster out to ∼2.2 r_{200} (∼4 Mpc). Our analysis of substructures reveals a complex system composed of a main massive cluster ($M_{200} \sim 0.9 \times 10^{15}\, M_\odot$ and $\sigma_{V,r200} \sim 1000\,\mathrm{km\,s^{-1}}$) presenting two major features: (i) a bimodal velocity distribution, showing two central peaks separated by $\Delta V_{\rm rf} \sim 1100\,\mathrm{km\,s^{-1}}$ with comparable galaxy content and velocity dispersion, and (ii) a projected elongation of the main substructures along the NE–SW direction, with a prominent sub-clump ∼600 kpc SW of the center and an isolated BCG approximately halfway between the center and the SW clump. We also detect a low-mass structure at $z \sim 0.390$, ∼10′ south of the cluster center, projected at ∼3 Mpc, with a relative line-of-sight velocity of $\Delta V_{\rm rf} \sim -1700\,\mathrm{km\,s^{-1}}$. The cluster mass profile that we obtain through our dynamical analysis deviates significantly from the "universal" NFW, being best fit by a Softened Isothermal Sphere model instead. The mass profile measured from the galaxy dynamics is found to be in relatively good agreement with those obtained from strong and weak lensing, as well as with that from the X-rays, despite the clearly unrelaxed nature of the cluster. Our results reveal an overall complex dynamical state of this massive cluster and support the hypothesis that the two main subclusters are being observed in a pre-collisional phase, in agreement with recent findings from radio and deep X-ray data. In this article, we also release the entire redshift catalog of 4386 sources in the field of this cluster, which includes 60 identified *Chandra* X-ray sources and 105 JVLA radio sources.

Key words: galaxies: clusters: general – galaxies: clusters: individual (MACS J0416.1-2403) – galaxies: distances and redshifts – galaxies: kinematics and dynamics

Supporting material: machine-readable tables

1. INTRODUCTION

According to the widely accepted "concordance model," i.e., a cold-dark-matter dominated model with a cosmological constant (ΛCDM), galaxy clusters form through gravitational collapse of the highest density peaks in the primordial density fluctuations of the universe and subsequent hierarchical assembly of smaller structures (e.g., Springel et al. 2006). As the largest structures in the universe which have had time to

[25] Hubble Fellow.

virialize at the current epoch and retain the different mass–energy density components in cosmological proportion, galaxy clusters represent important probes for cosmology, as well as unique natural laboratories for galaxy evolution and structure formation (e.g., Dressler 1984; Kravtsov & Borgani 2012 and references therein).

One of the key predictions of *N*-body simulations is the self-similarity of dark matter halos, which are expected to follow a "universal" density profile (Navarro et al. 1996, 1997, hereafter NFW). Good data quality and complementary mass probes are fundamental to observationally test these theoretical predictions. First results based on combined strong-lensing (SL) and weak-lensing (WL) mass reconstruction were controversial, finding both agreement with the NFW profile (e.g., Broadhurst et al. 2005a, 2005b; Zitrin et al. 2009; Umetsu et al. 2010) and deviations from it (e.g., Newman et al. 2009). Deviations from the NFW profile seem to become apparent only at scales $<$30 kpc around the brightest central galaxy (BCG) and if the dark matter and baryonic components can be disentangled (Newman et al. 2009, 2013). The combination of different, complementary probes, such as lensing, stellar kinematic of the BCG, dynamics of cluster galaxies, and X-ray surface brightness, allows for the reconstruction of the total mass profile of a cluster over wide ranges of cluster-centric distances, while keeping under control all of the systematics inherent to the different probes (e.g., Newman et al. 2009, 2011; Biviano et al. 2013; von der Linden et al. 2014).

With the aim of precisely characterizing the mass profiles of galaxy clusters using lensing, a sample of 25 massive clusters (20 selected as relaxed clusters based on their X-ray morphology and 5 selected as high-magnification lensing clusters) has been observed with the *Hubble Space Telescope* (*HST*) as part of the Multi-Cycle Treasury program Cluster Lensing And Supernova survey with Hubble (CLASH; P.I.: M. Postman; Postman et al. 2012). The *HST* survey, nicely complemented by Subaru wide-field imaging, has allowed for significant improvement in reconciling theoretical predictions for the shape of the mass profile and for the mass–concentration relation with observations (Meneghetti et al. 2014; Umetsu et al. 2014; Merten et al. 2015).

Targeting 14 of the southern CLASH clusters, our extensive spectroscopic campaign carried out with the Very Large Telescope (VLT; CLASH-VLT Large Programme 186.A-0.798; P.I.: P. Rosati; Rosati et al. 2014) is currently providing thousands of spectroscopic redshifts for cluster member galaxies and other intervening structures along the line of sight, including high-z, highly magnified, lensed background galaxies (see Balestra et al. 2013; Biviano et al. 2013; Girardi et al. 2015; Grillo et al. 2015).

In the first CLASH-VLT cluster analyzed (MACS J1206.2-0847 at $z = 0.44$), the unprecedented number of spectroscopic redshifts of member galaxies out to the cluster outskirts ($\sim$5 Mpc) has allowed us to perform a mass profile reconstruction through galaxy dynamics well beyond the cluster virial radius (see Biviano et al. 2013). In that fairly relaxed cluster, the mass profile obtained from the dynamical analysis is found to be in extremely good agreement with that derived from all of the other independent probes (i.e., SL, WL, and X-rays) over two decades in radius and consistent with NFW.

The combination of high-quality *HST* and Subaru imaging with the large VLT spectroscopic follow-up has allowed significant progress in many aspects of our understanding of galaxy cluster formation and evolution: new constraints on velocity anisotropies and pseudo-phase-space density profiles (Biviano et al. 2013), the contribution of mergers of different mass to cluster growth (Lemze et al. 2013), the pressureless nature of dark matter (Sartoris et al. 2014), precise mass profiles from WL (Umetsu et al. 2014), the mass–concentration relation (Meneghetti et al. 2014; Merten et al. 2015), substructures and galaxy populations (Girardi et al. 2015), precise stellar mass functions and stellar mass density profiles (Annunziatella et al. 2014), and the effect of the environment on galaxy evolution (Annunziatella et al. 2016).

MACS J0416.1-2403 (hereafter MACS0416; Ebeling et al. 2001) is a massive, X-ray luminous ($L_X \sim 10^{45}$ erg s^{-1}) galaxy cluster at $z \simeq 0.4$. Selected as one of the 5 clusters with high magnification in the CLASH sample, MACS0416 was first imaged by *HST* for 25 orbits using 16 filters as part of the CLASH survey (Postman et al. 2012), where the *HST* mosaics were produced following the approach described in Koekemoer et al. (2011). The cluster was subsequently re-observed as part of the Hubble Frontier Fields (HFF) initiative (Koekemoer et al. 2014; Lotz et al. 2014) for 140 orbits in 7 filters, achieving in all of them a 5σ point-source detection limit of $\simeq$29 mag (AB).

Early works based on relatively shallow *Chandra* observations identified MACS0416 as a merger, possibly in a post-collisional phase, given its unrelaxed X-ray morphology and the observed projected separation ($\sim$200 kpc) of the two brightest cluster galaxies (BCGs; see Mann & Ebeling 2012).

The first SL analysis performed by Zitrin et al. (2013) using CLASH *HST* data showed a quite elongated projected mass distribution in the cluster core ($\sim$250 kpc). Combining WL and SL analyses, Jauzac et al. (2015) detected two main central mass concentrations, as well as two possible secondary ones to the SW and NE, both at $\sim 2'$ from the cluster center. Comparing their mass reconstruction with the position of the X-ray peaks from the early, shallow *Chandra* observations, they measured some offset ($\sim 15''$) between one of the dark matter concentrations and the position of the intra-cluster gas; however, this did not allow them to unambiguously discern between a pre-collisional or post-collisional merging scenario.

Thanks to the large number of our CLASH-VLT spectroscopic redshifts for the member galaxies and multiply imaged lensed objects, and thanks to a novel technique for identifying cluster members using multi-dimensional *HST* color-space information, our group has been able to significantly improve the SL model used for mass reconstruction and was also able to derive a precise characterization of the sub-halo mass function in the core of MACS0416 (Grillo et al. 2015). The new high-resolution mass model currently represents the most precise mass reconstruction available for this FF cluster. The model is composed of 2 cored elliptical dark matter halos plus carefully modeled galaxy halos around 175 cluster members in the core. The two extended halos are significantly separated from the centers of the two BCGs (with projected distances of $\sim$50 and $\sim$30 kpc from the NE- and SW-BCG, respectively) and they are separated by a total projected distance of $\sim$300 kpc.

Recently, Ogrean et al. (2015) compared new, deeper *Chandra* observations with JVLA radio data and SL mass reconstruction, finding no offset between dark matter and hot baryons, as well as an X-ray cavity, lacking radio emission, which is close to the NE-BCG. These findings lead to the conclusion that a pre-collisional merging scenario could be

Table 1
Log of VIMOS Observations of the Frontier Fields Cluster MACS J0416.1-2403, Taken as Part of our CLASH-VLT Spectroscopic Campaign

Mask ID (1)	Date (2)	Exp. Time (s) (3)
Low-resolution masks		
MOS_M0416_LRB_1_M1r	2012 Dec	3 × 1200
MOS_M0416_LRB_3_M1	2012 Dec	3 × 1200
MOS_M0416_LRB_2_M1r	2013 Jan	3 × 1200
MOS_M0416_LRB_1_M2	2013 Feb	2 × 900
MOS_M0416_LRB_4_M2	2013 Feb	2 × 900
MOS_M0416_LRB_4_M1	2013 Feb	3 × 1200
MOS_M0416_LRB_3_M2	2013 Feb	3 × 1200
MOS_M0416_LRB_2_M2	2013 Feb	3 × 1200
MOS_M0416_LRB_2_M2_2	2013 Sep	3 × 1200
MOS_M0416_LRB_1_M3	2013 Oct	3 × 1200
MOS_M0416_LRB_2_M3	2013 Oct	3 × 1200
MOS_M0416_LRB_3_M2_2	2013 Nov	3 × 1200
MOS_M0416_LRB_3_M3	2014 Jan	3 × 1200
MOS_M0416_LRB_4_M1_2	2014 Jan	3 × 1200
MOS_M0416_LRB_4_M3	2014 Jan	3 × 1200
Medium-resolution masks		
MOS_M0416_MR_1_M3	2014 Jan	3 × 1200
MOS_M0416_MR_2_M3	2014 Jan	3 × 1200
MOS_M0416_MR_4_M3	2014 Feb	3 × 1200
MOS_M0416_MR_3_M3	2014 Feb	3 × 1200
MOS_M0416_MR_1_M4	2014 Sep	3 × 800
MOS_M0416_MR_4_M4	2014 Nov	3 × 1200

Note. Columns list the following information: (1) mask identification number, (2) date of the observations, and (3) number of exposures and integration time of single exposures.

more likely, but did not exclude a post-collisional configuration.

In this paper, we exploit our extensive VLT spectroscopic follow-up campaign to investigate in detail the dynamical state of this complex merging cluster and to a derive precise mass profile from the cluster dynamics out to large radii, which we also compare with other available mass probes, to provide a very precise mass characterization over a wide range of cluster-centric distances.

The plan of the paper is as follows. In Section 2, we describe the sample and its photometric and spectroscopic data. In Section 3, we describe the selection of cluster members and, in Section 4, we describe the structural analysis of the cluster. The results of our dynamical analysis and the mass profile derived from it are presented in Section 5. In Section 6, we discuss our results and we summarize our conclusions in Section 7.

Throughout the paper, magnitudes are given in the AB system ($\mathrm{AB} \equiv 31.4\text{–}2.5\ \log\langle f_\nu/\mathrm{nJy}\rangle$) and errors at the 68% confidence level, unless otherwise stated. We assume a cosmology with Ω_{tot}, Ω_M, $\Omega_\Lambda = 1.0$, 0.3, 0.7, and $H_0 = 70\,\mathrm{km\,s^{-1}\,Mpc^{-1}}$. In the adopted cosmology, 1′ corresponds to ∼321 kpc at the cluster redshift.

2. THE DATA SAMPLE

2.1. CLASH-VLT Spectroscopy with VIMOS

The cluster MACS J0416.1-2403 was observed between 2012 December and 2014 November as part of the ESO Large Programme 186.A-0798 "Dark Matter Mass Distributions of Hubble Treasury Clusters and the Foundations of ΛCDM Structure Formation Models" (P.I.: Piero Rosati) using VIMOS (Le Fèvre et al. 2003) at the ESO VLT. The log of our CLASH-VLT observations of this cluster is presented in Table 1. The VIMOS observations were designed in sets of four separate pointings, each with a different quadrant centered on the cluster core. The overlapping quadrants on the cluster core were used both to achieve longer integration times on faint arcs and other interesting SL features, and to have the largest possible number of slits on candidate cluster members in the crowded central region of the cluster.

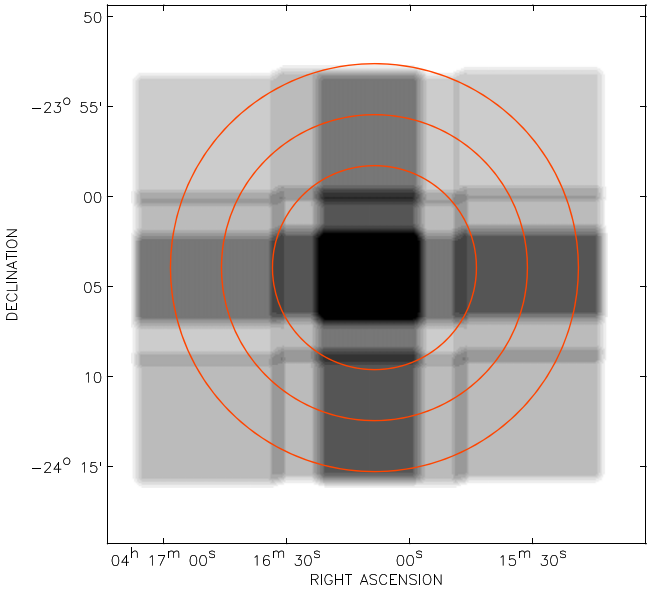

Figure 1. Footprint of our CLASH-VLT spectroscopic observations shown as the resulting "exposure map" of the 21 VIMOS pointings in the field of MACS0416. The size of the footprint is 26′ × 23′. The three red circles are centered on the NE-BCG and have radii of 1, 1.5, and 2 r_{200} (where $r_{200} = 1.82$ Mpc).

A total of 21 masks were observed (15 LR-Blue masks and 6 MR masks). Each mask has an integration time of 1 hr (split into 3 × 20 minute OBs), with the exception of 3 masks which have integration times of 30 and 40 minutes (see Table 1). The footprint of our CLASH-VLT spectroscopic observations is displayed in Figure 1 which also shows the resulting "exposure map" of the 21 VIMOS pointings.

The LR-Blue masks cover the spectral range 3700–6700 Å with a resolution of $R = 180$, while the MR masks cover the range 4800–10000 Å with a resolution of $R = 580$. The width of the slits is set to 1″. To maximize the number of targets per pointing, both in the LR-Blue and the MR masks, we used shorter-than-standard slits (down to 6″). This has the advantage of improving multiplexing (we are able to fit up to 140 slits in a single quadrant, i.e., more than 500 targets per mask) without compromising sky subtraction (see Scodeggio et al. 2009).

Data reduction has been performed using the VIMOS Interactive Pipeline Graphical Interface (VIPGI, Scodeggio et al. 2005), which follows standard MOS data reduction steps (e.g., bias subtraction, flat-field correction, bad-pixel cleaning, sky subtraction, fringing correction, wavelength calibration).

Redshift determination was performed following a two-step procedure similar to that used in Balestra et al. (2010):

1. we first ran the *EZ* software (Garilli et al. 2010) for automatic cross-correlation with template spectra (i.e.,

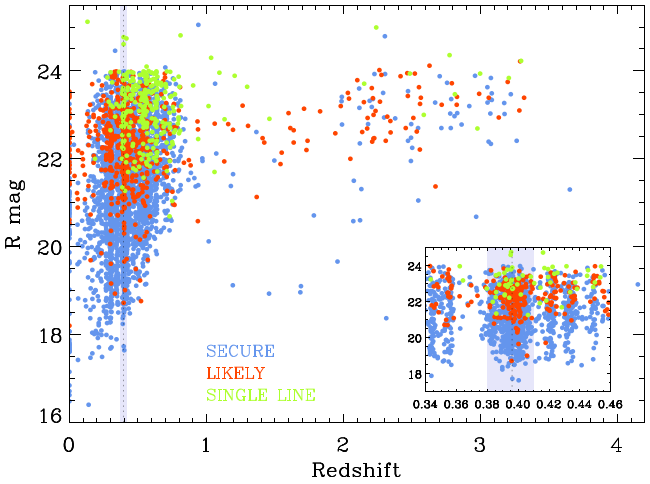

Figure 2. Subaru R-band magnitude vs. redshift for all of the galaxies with reliable spectroscopic redshift. Data points are plotted in different colors according to the reliability classes of the spec-z, as defined in the text. The vertical dotted line marks the mean redshift of galaxies in MACS0416. The gray shaded area indicates the redshift interval corresponding to rest-frame LOS velocities of ± 3000 km s^{-1}. The inset is a zoom around the redshift of MACS0416.

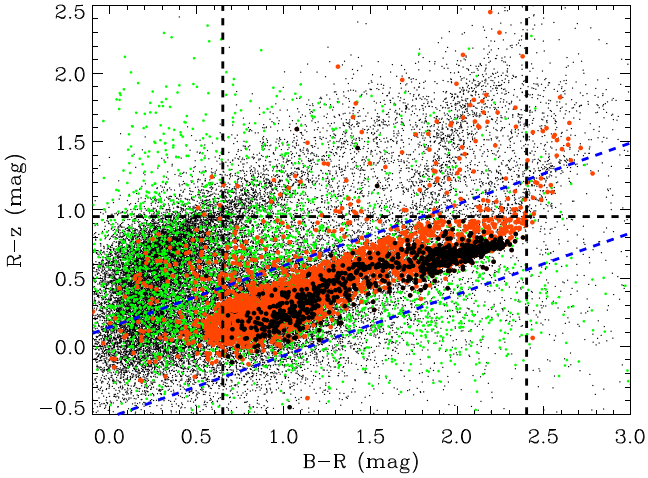

Figure 3. Subaru Rc–z vs. B–Rc colors for all of the sources with Rc magnitudes <24. The dashed lines show the color cuts defining the box used for target selection. Small black dots refer to the Subaru photometric catalog. Larger colored data points mark objects belonging to our CLASH-VLT spectroscopic catalog (stars in green, cluster member galaxies in black, all the rest in red).

ordinary S0, Sa, Sb, Sc, and elliptical galaxies at low redshift, Lyman break galaxies, and quasars at high redshift);
2. we visually inspected redshift solutions obtained in the first step and we modified the most obvious failures where more than two spectral features could be unambiguously identified.

During the visual check, we also assign a Quality Flag (QF) to each redshift, which qualitatively indicates the reliability of a redshift measurement. We define four redshift quality classes using the following criteria:

1. "Secure" (QF = 3), several emission lines and/or strong absorption features are clearly identified;
2. "Likely"(QF = 2), intermediate-quality spectra where at least two spectral features are well identified, for instance, one emission line plus at least one absorption feature;
3. "Insecure" (QF = 1), low signal-to-noise ratio spectra, i.e., spectral features, either in emission or in absorption, are less clearly identified;
4. "Emission-line" (QF = 9), redshift based on a single emission line only.

To assess the reliability of these four quality classes, we compared pairs of duplicate observations having at least one secure measurement. In this way, we could quantify the reliability of each quality class as follows: redshifts with QF = 3 are correct with a probability of >99.99%, QF = 9 with ∼92% probability, QF = 2 with ∼75% probability, and QF = 1 with <40% probability. In this paper, we will only consider redshifts with QF = 3, 2, and 9.

The final spectroscopic data set contains a total of 4386 reliable redshifts within an area of 26 × 23 arcmin around the center of the cluster, covering almost the entire Subaru field of view. In Figure 2, we plot the Subaru R-band magnitude as a function of the spectroscopic redshift for the entire CLASH-VLT sample of objects in the field of MACS0416.

2.2. Target Selection

Targets were selected through specifically defined cuts in the color–color space using Subaru photometry. Figure 3 shows the selection box in the Rc–z versus B–Rc (Subaru bands) diagram, which we adopted for our search of cluster members. The adopted cuts are the following:

1. $-0.52 + 0.45(B - Rc) < Rc - z < 0.14 + 0.45 (B - Rc)$;
2. $0.65 < B - Rc < 2.40$;
3. $Rc - z < 0.95$;
4. $18.0 < Rc < 24.0$.

These color cuts have been chosen in order to maximize the success rate in cluster member selection, while at the same time keeping the number of contaminants low and allowing for the inclusion of blue, star-forming cluster members in the spectroscopic sample. Note that a fraction of objects with spectroscopic redshifts fall outside the selection box in Figure 3. These are mostly sources that have been manually inserted in slits, serendipitous objects found in some slits, and a few objects with redshifts from the literature (Ebeling et al. 2014, D. Kelson 2016, private communication). In addition to cluster members, we also targeted multiply imaged lensed galaxies or other SL features, high-z candidates (e.g., dropout from Bradley et al. 2014) with $z_{\rm phot} \lesssim 7$, a few possible supernova hosts (e.g., Patel et al. 2014), and all of the *Chandra* sources in the field. Obviously, all of these sources may also lie outside the selection box.

2.3. Catalog of Spectroscopic Redshifts

In our released CLASH-VLT spectroscopic redshift catalog (see Table 2), for each object we provide the following: (Column 1) coordinate-based CLASH-VLT identification number, (Columns 2, 3) coordinates (Subaru Suprime-Cam WCS), (Column 4) spectroscopic redshift, (Column 5) redshift QF, as described in Section 2.1, (Column 6) reference for the redshift (i.e., CLASH-VLT VIMOS [4370 redshifts]: 1—based on LR-

Table 2
CLASH-VLT Spectroscopic Redshift Catalog of MACS J0416.1-2403

ID	R.A.	decl.	z	QF	Ref.	Mag
(1)	(2)	(3)	(4)	(5)	(6)	(7)
CLASHVLTJ041531.2-241516	63.879843	−24.254507	0.4648	3	1	19.32
CLASHVLTJ041615.9-241539	64.066112	−24.261057	0.3448	3	1	19.92
CLASHVLTJ041614.3-241542	64.059571	−24.261808	0.3021	3	1	20.93
CLASHVLTJ041654.3-241545	64.226374	−24.262606	0.3078	3	1	21.94
CLASHVLTJ041521.3-241510	63.838858	−24.252900	0.3009	3	1	19.60
CLASHVLTJ041610.1-241543	64.041928	−24.262141	0.7231	3	1	21.95
CLASHVLTJ041543.4-241517	63.930875	−24.254946	0.1902	3	1	19.56
CLASHVLTJ041614.1-241547	64.058570	−24.263075	0.3009	3	1	22.61
CLASHVLTJ041632.5-241547	64.135563	−24.263133	0.5082	3	1	23.06
CLASHVLTJ041619.0-241545	64.079154	−24.262658	0.2999	2	1	22.37

Note. The entire table is available as supplementary material in the Astrophysical Journal Supplement Series, on CDS, and at following URL: https://sites.google.com/site/vltclashpublic/. The full table contains 7 columns and 4386 redshifts. Columns list the following information: (1) VIMOS identification number, (2–3) coordinates, (4) spectroscopic redshift, (5) redshift quality flag, (6) reference (i.e., CLASH-VLT VIMOS [4370 redshifts]: 1—based on LR-Blue spectra [3582], 2—based on MR spectra [486], 3—based on a combination of LR-Blue and MR spectra [302], 4—Ebeling et al. (2014) [5], 5—*Magellan* (D. Kelson 2016, private communication) [11]), and (7) Subaru R-band magnitude.

(This table is available in its entirety in machine-readable form.)

Blue spectra [3582], 2—based on MR spectra [486], 3—based on a combination of LR-Blue and MR spectra [302], 4—Ebeling et al. (2014) [5], 5—*Magellan*, (D. Kelson 2016, private communication) [11]), and (7) Kron R-band magnitude (AB, Subaru Suprime-Cam). The spectroscopic redshift catalog is made publicly available to the scientific community.[26] For repeated observations of the same objects, the catalog provides a mean value of the redshift measurements. Uncertainties on the redshifts vary between 75 and 150 km s^{-1}, depending on the spectral resolution and on the number and resolution of the spectra upon which the mean redshift is computed (see also Biviano et al. 2013). This catalog also includes redshifts of arcs and lensed, multiply imaged sources used in the SL mass reconstruction presented by Grillo et al. (2015). The total number of objects in our released catalog is 4386, including 5 redshifts from the literature (Ebeling et al. 2014) and 11 unpublished redshifts from *Magellan* observations (D. Kelson 2016, private communication). The number of VIMOS spectra obtained with the MR grism amounts to ∼15% of the total. In the released catalog, where a single entry is preserved in case of duplicate observations of the same object, 3582 redshifts are measured from LR-Blue spectra, 486 from MR spectra, and 302 from a combination of LR-Blue and MR spectra.

2.4. Completeness of the Spectroscopic Catalog

The inhomogeneity and incompleteness of a spectroscopic sample may affect our ability to detect substructures in galaxy clusters, as well as the determination of the projected number density of cluster galaxies, which is used to reconstruct the cluster mass profile from the kinematics. We checked the completeness of our spectroscopic catalog both as a function of position on the sky and of magnitude. Figure 4 shows the completeness map of our spectroscopic catalog, which we computed as the ratio of the two-dimensional (2D) density of those objects for which we were able to obtain a redshift over the 2D density of the targeted objects. This plot shows how the completeness of our spectroscopic sample is relatively uniform across the field observed, declining only at the corners and beyond $\sim 2r_{200}$. As can be inferred from this map, the completeness is approximately constant as a function of radius out to $\sim 2r_{200}$. The dependence of the completeness on magnitude follows very closely that derived for the first CLASH-VLT cluster analyzed (see Figure 4 in Biviano et al. 2013).

3. SELECTION OF CLUSTER MEMBERS

We will now describe the procedure used for the identification of cluster member galaxies in MACS0416. Cluster members were selected among the 4386 galaxies with reliable spectroscopic redshifts by applying the two-steps method "peak +gap" (P+G), which was also used for the dynamical analysis of the CLASH cluster MACS J1206.2-0847 in Biviano et al. (2013) and in Girardi et al. (2015). This method is a combination of 1D-DEDICA (Pisani 1993, 1996), which is an adaptive kernel method for the evaluation of the density probability function underlying an observational discrete data set, and the "shifting gapper" method, which uses both position and velocity information (Fadda et al. 1996; Girardi et al. 1996).

In the redshift distribution of our spectroscopic data of MACS0416, the 1D-DEDICA procedure detects two largely overlapped peaks at $z \sim 0.396$ and $z \sim 0.400$, which are composed of 428 and 401 galaxies, respectively (see Figure 5).

The second step of our member-selection procedure consists of rejecting galaxies with line-of-sight velocities that are too far off the main body of galaxies ($V = cz$). This is done by considering a fixed bin that shifts along the distance from the cluster center. The procedure is iterated until the number of cluster members converges. We used a velocity gap of 500 km s^{-1} in the cluster rest-frame and a bin of 0.4 Mpc, or large enough to include at least 15 galaxies. Note that the parameters adopted here are much more stringent than those originally used in Fadda et al. (1996), owing to the much better sampling and much higher density of the galaxies in our spectroscopic sample.

Given the complex structure of the core, with two BCGs and two extended dark matter halos separated by ∼40″–50″ and

[26] The full CLASH-VLT spectroscopic catalog is publicly available in the Astrophysical Journal Supplement Series, on CDS, and at the following URL: https://sites.google.com/site/vltclashpublic/

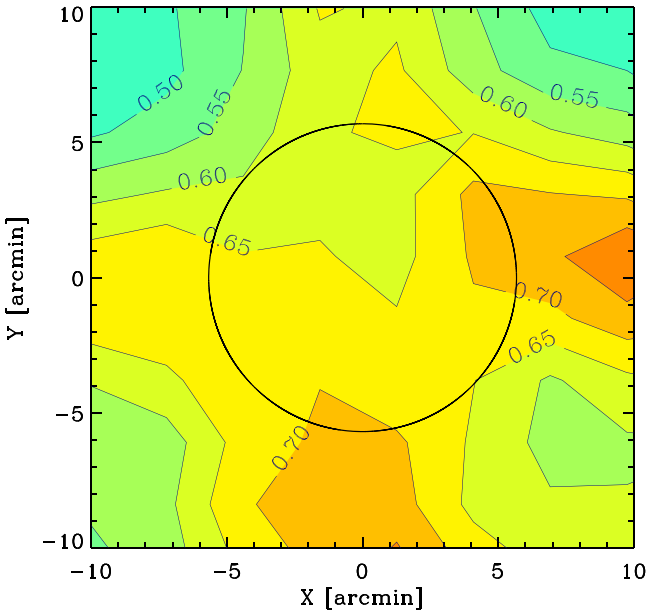

Figure 4. Completeness map of our CLASH-VLT spectroscopic sample. The contour levels are labeled with the value of completeness. Overall, the completeness is relatively uniform, being mostly between 0.5 and 0.7 and declining only at the corners of the field observed, beyond $\sim 2r_{200}$. The black circle shows the size of the cluster virial radius, $r_{200} = 1.82$ Mpc.

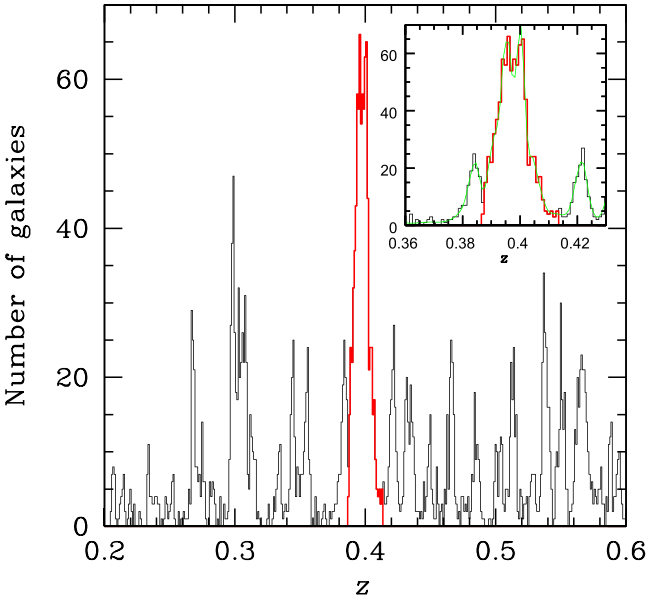

Figure 5. Redshift distribution of the whole sample of galaxies with spectroscopic redshift $0.2 < z < 0.6$ (black histogram). The 829 galaxies assigned to MACS0416 according to the DEDICA reconstruction method are shown in red. The inset shows a zoom in the distribution around the peak with the DEDICA reconstruction superimposed (green).

aligned along the NE–SW direction, defining the center of the cluster is not simple. As shown in Grillo et al. (2015), the barycenter of the cluster lies approximately halfway along the line connecting the two BCGs (R.A. = 04:16:08.60, decl. = −24:04:25.2), ∼23″ from NE-BCG. However, the X-ray emission clearly shows a more prominent peak coincident with the position of the NE-BCG (see Ogrean et al. 2015). We decided to adopt the position of the NE-BCG and the peak of the X-ray emission (R.A. = 04:16:09.14,

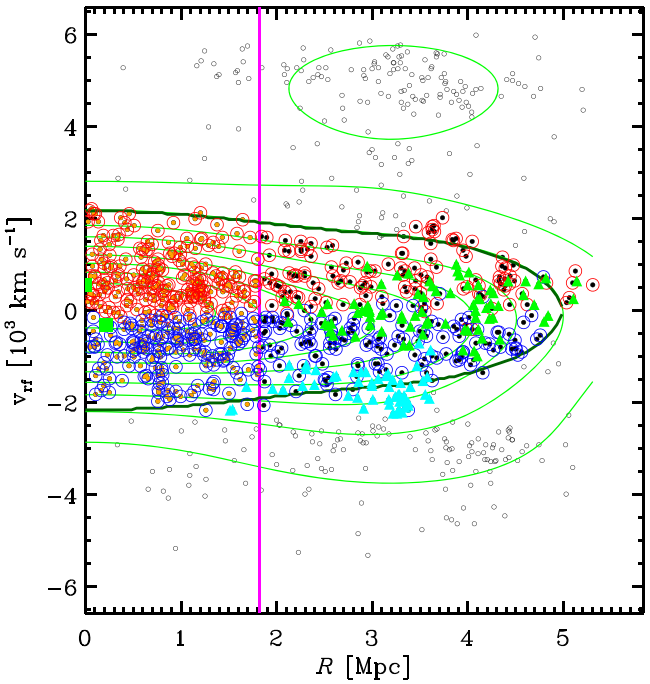

Figure 6. Projected phase-space diagram: rest-frame velocities are plotted as a function of the projected radii. Filled dots identify galaxies selected as cluster members. Blue and red circles mark galaxies in the two main subclusters. Cyan triangles indicate fiducial members belonging to the Sext group, while green triangles are for galaxies of the less prominent W substructure detected in the 3D analysis described in Section 4. The two green squares mark the positions of the two BCGs. The vertical magenta line indicates the value of $r_{200} = 1.82$ Mpc, obtained from the weak-lensing analysis by Umetsu et al. (2014). The green curves show the isodensity contours and the thick dark-green line is the Caustic selected for our dynamical analysis (see Section 5).

decl. = −24:04:03.1) as the center of the cluster throughout our analysis. With this choice of the center, the second step of our member-selection procedure rejects 48 galaxies. The remaining 781 galaxies represent our fiducial sample of cluster members. Figure 6 shows the projected phase-space diagram (i.e., rest-frame line-of-sight velocities versus projected radii) and the isodensity contours (i.e., "Caustics").

We also verified that for different choices of the center, galaxies identified as cluster members do not vary significantly. For example, if the center is fixed on the position of the barycenter (Grillo et al. 2015), then the galaxies identified as members are identical to those of our fiducial sample, except for about 10 galaxies (∼1%), which all lie at radii larger than 5′. Therefore, the exact choice of the center has little influence on the results of our dynamical analysis. Figure 6 also highlights the large velocity difference between the two BCGs ($\Delta V_{\rm rf} \sim 900$ km s^{-1} in the velocity rest-frame).

By applying the biweight estimator (Beers et al. 1990) to the 781 cluster members of the whole system, we obtain a mean cluster redshift of $\langle z \rangle = 0.3972 \pm 0.0001$. We estimate the line-of-sight velocity dispersion, σ_V, by using the biweight estimator and by applying the cosmological correction and the standard correction for velocity errors (Danese et al. 1980). We obtain $\sigma_V = 996^{+12}_{-36}$ km s^{-1}, where errors are estimated using a bootstrap technique. Table 3 lists the kinematical properties of the whole sample of cluster members, as well as those of the main system (MS) and the prominent southern external substructure (Sext) as discussed in the following section.

Table 3
Kinematical Properties of the Whole Cluster Sample, the Main Sample (MS), and the Southern External Structure (Sext)

Sample	N_g	$\langle V \rangle$ (km s^{-1})	σ_V (km s^{-1})
(1)	(2)	(3)	(4)
Whole Sample	781	119083 ± 36	996^{+12}_{-36}
MS[a]	728	119233 ± 34	919^{+16}_{-30}
Sext	53	116869 ± 47	336^{+17}_{-47}

Notes. Columns list the following information: (1) id of the subsample, (2) number of galaxies, (3) average velocity, and (4) velocity dispersion.
[a] When restricting the analysis to galaxies of the MS within r_{200}, we measure $\sigma_V = 998^{+25}_{-39}$ km s^{-1}.

4. STRUCTURAL ANALYSIS

In this section, we investigate the complex structure of the cluster using the large spectroscopic sample of cluster members to determine the presence of substructures within the cluster.

The first, clearly apparent feature of the cluster structure is a bimodality of the velocity distribution of the cluster members. The bimodality is evident both in the whole galaxy sample and in the subsample of cluster members within the virial radius. This is illustrated in Figure 7, which shows a histogram of the velocity distribution of the 388 cluster galaxies lying within r_{200} together with the 1D-DEDICA reconstruction. The 1D-DEDICA method assigns 181 and 207 members to the low- and high-velocity subcluster, respectively. The two subclusters, which are largely overlapping (having 238 out of the 388 galaxies in common), peak at $z = 0.395$ and $z = 0.400$, respectively. Their redshift difference corresponds to $\Delta V_{\rm rf} \sim 1100$ km s^{-1}. Table 3 lists the kinematical properties of the whole sample of cluster members, as well as those of the MS and the prominent Sext, separately.

We also applied the Kaye's mixture model (KMM) test (Ashman et al. 1994; Girardi et al. 2008), which favors a two-group partition over a single Gaussian, extracting two groups of comparable galaxy content and velocity dispersion ($\sim$700 km s^{-1}) at the $\sim$95% confidence level. Both BCGs have a significant peculiar velocity (>99% c.l.) with respect to the velocity distribution of the galaxy sample within r_{200} according to the indicator test by Gebhardt & Beers (1991).

We used the 2D-DEDICA method to detect density peaks in projection on the plane of the sky. In Figure 8 (upper panel), we plot the spatial distribution on the sky and isodensity contours of the 781 spectroscopic members of MACS0416. This plot highlights the complex 2D structure of MACS0416 and the presence of a density peak in the Sext substructure. Table 4 lists the results of the 2D-DEDICA analysis for the four peaks with relative density $\rho_S > 0.2$ within r_{200} (C, SW, NE1, NE2), and the densest peak outside r_{200} (Sext).

The presence of the Sext structure is also shown by our analysis of the combined three-dimensional (3D) information of the projected positions and line-of-sight velocity. We used a modified version of the Dressler & Shectman (1988) test where the mean velocity is considered separately from the velocity dispersion (hereafter DS$\langle V \rangle$-test). This test considers the deviations of the local mean velocities from the global mean velocity, $\delta_{V,i}$, where the deviation is computed on the group formed by the ith galaxy and its 10 closest neighbors (e.g., Girardi et al. 1997; Biviano et al. 2002; Ferrari et al. 2003; Girardi et al. 2010, 2014). The DS$\langle V \rangle$ test detects significant substructures at >99.9% c.l. using 1000 Monte Carlo simulated clusters. Figure 9 shows in a color-coded plot the resulting distribution of the local mean-velocity deviations ($\delta_{V,i}$). The Sext structure clearly stands out because of its low velocity and it appears elongated toward the MS, while the main cluster is elongated along the NE–SW direction.

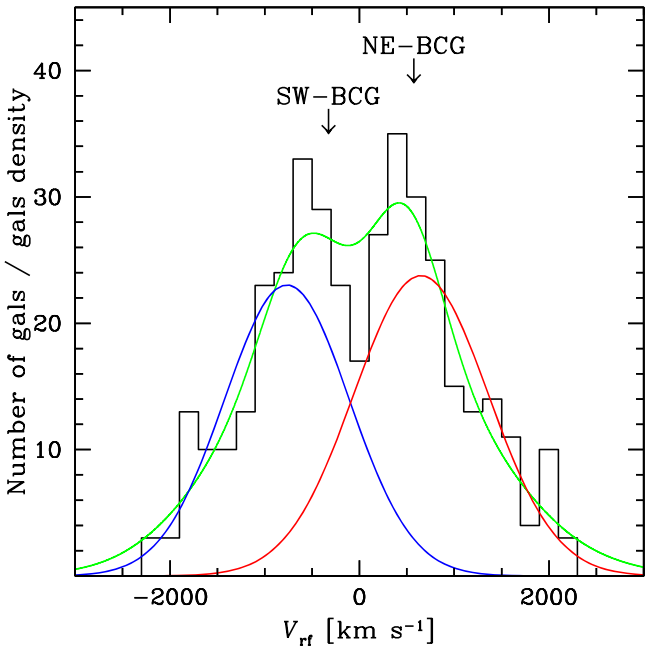

Figure 7. Rest-frame velocity distribution and 1D-DEDICA density reconstruction for all the galaxies within r_{200} (black histogram and green curve). The two arrows indicate the velocities of the two BCGs. The two Gaussians obtained by applying the KMM method are also displayed (blue and red curves).

We applied the 3D-DEDICA method (Pisani 1993, 1996) to the full spectroscopic sample. This method leads to a very complex description of the cluster structure, detecting 18 groups that are statistically significant at $\gtrsim$99.99% c.l., having at least 10 galaxies, and with a relative density larger than 0.2, plus a plethora of less significant groups. In order to refine the identification of galaxies of the Sext structure and, consequently, to obtain a "cleaner characterization" of the MS, we ran an alternative 3D analysis using a simplified version of the 3D-DEDICA method. Our simplified version is based on the same definition of the adaptive kernel estimate of Pisani (1993, 1996), in particular, with the same computation of the local bandwidth factor λ_i (see Equations (26) and (27) in Pisani 1993), but where the size parameter σ is not estimated using the recursive procedure of Pisani (1993, 1996, see their method to obtain σ_n). Instead, we adopted the rule-of-thumb value, $\sigma \sim 2.6\sigma_n$, proposed by Silverman (1986). We stress that our simplified procedure, while still using an adoptive kernel method, is optimized to trace mainly the large-scale structure of the cluster. The simplified procedure is successful in recovering the Sext structure (53 galaxies), as well as two main subclusters at low (Lo-V, 316 galaxies) and high velocity (Hi-V, 331 galaxies) with $\Delta V_{\rm rf} \sim 1200$ km s^{-1}, plus a minor, less-concentrated western structure (W, 81 galaxies), whose relative density is only $\sim$10%, reported here for the sake of completeness. Table 5 lists the properties of the four substructures detected by our 3D analysis. The spatial

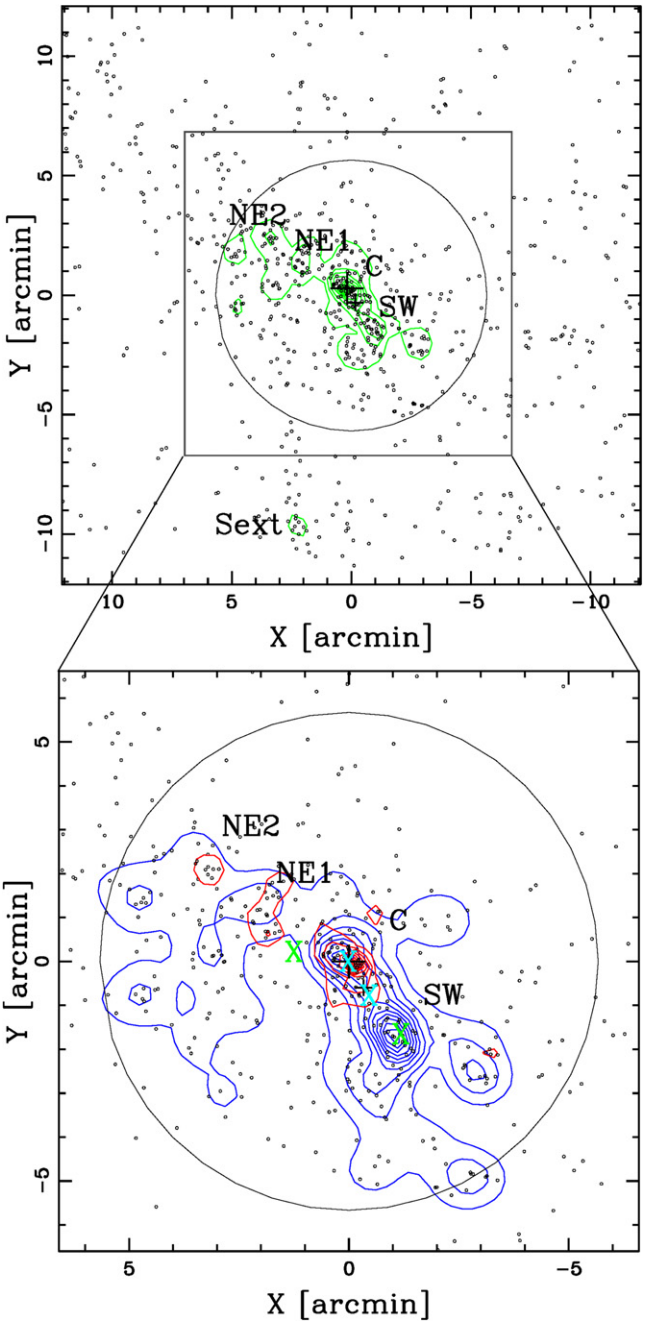

Figure 8. Upper panel: spatial distribution on the sky and relative isodensity contour map of the 781 spectroscopic members of MACS0416 (Whole Sample), obtained with the 2D-DEDICA method. The positions of the two BCGs (NE-BCG and SW-BCG) are indicated with two black crosses. The labels mark the five main density peaks detected by 2D-DEDICA (see also Table 4). Lower panel: a zoomed-in version of the same plot within the virial region, where blue and red contours mark the isodensity of galaxies in the low- and high-velocity subcluster, respectively. Green "X" symbols indicate the positions of the two mass concentrations detected though gravitational lensing by Jauzac et al. (2015; S1 at SW and S2 at NE) and cyan "X" symbols mark the position of the two peaks in X-ray emission following Ogrean et al. (2015). For visual reference, we also plot a circle of radius $r_{200} = 1.82$ Mpc, as obtained from the weak-lensing analysis by Umetsu et al. (2014).

distribution of these substructures is shown in Figure 10 (see also Figure 6, where the same colors are used for the four substructures).

We assume that the MS is formed by the two main subclusters plus the smaller W structure. The two main

Table 4
2D-DEDICA Results on the Detection of Spatial Substructure in the Whole Sample of Cluster Members

Sub-clump	N_S	α(J2000)	δ(J2000)	ρ_S	χ^2_S
(1)	(2)	(3)		(4)	(5)
C	104	04:16:08.6	−24:04:07	1.00	55
SW	47	04:16:04.2	−24:05:46	0.42	25
NE1	44	04:16:17.7	−24:02:59	0.28	21
NE2	25	04:16:23.3	−24:01:57	0.24	13
Sext	29	04:16:18.2	−24:14:01	0.13	12

Note. Columns list the following information: (1) id of sub-clump, (2) number of assigned members, (3) coordinates of the density peak, (4) density relative to the densest peak, and (5) χ^2 value for each peak.

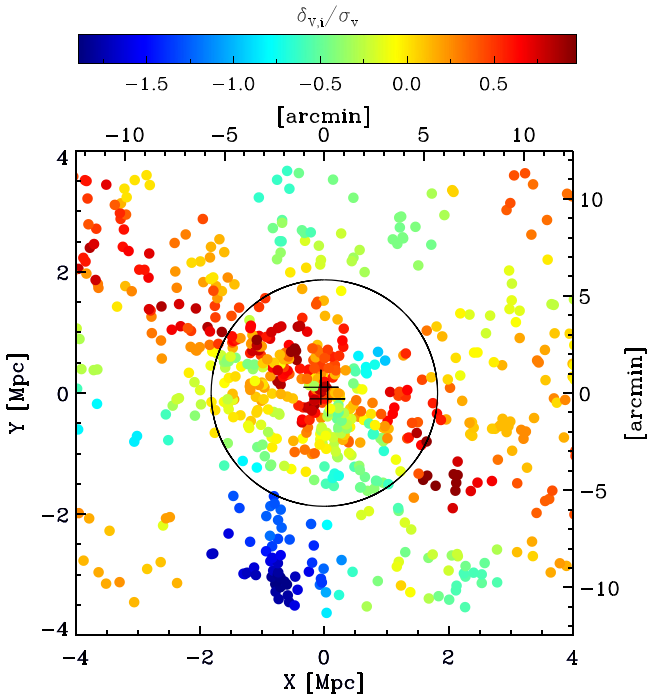

Figure 9. Spatial distribution of the 781 cluster member galaxies of the whole system color-coded according to the weighting parameter $\delta_{V,i}/\sigma_V$, where $\delta_{V,i}$ is the difference between the local mean velocity (computed on a group formed by the ith galaxy and the 10 nearest neighbors) and the global mean velocity (see also Section 3). The positions of the two BCGs are marked with two black crosses. For visual reference, we plot a circle of radius equal to $r_{200} = 1.82$ Mpc.

subclusters have similar galaxy content (∼300 galaxies) and roughly similar velocity dispersion $\sigma_V \sim 500$–$550\,\mathrm{km\,s^{-1}}$. Given the cluster mass computed within $r_{200} = 1.82$ Mpc (see Section 5), if simply scaling the virial mass by σ_V^2, from the measured σ_V for the two subclusters we obtain masses of ~ 3–$4 \times 10^{14}\,M_\odot$ within the virial region. The Sext structure lies at $\Delta z \sim -0.008$ from the MS, corresponding to a rest-frame velocity of $\Delta V_{\rm rf} \sim -1700\,\mathrm{km\,s^{-1}}$, and it is a low-mass structure, as indicated by the velocity dispersion of its galaxies ($\sigma_{V,\rm Sext} \sim 300\,\mathrm{km\,s^{-1}}$, corresponding to a virial mass of $\sim 2 \times 10^{13}\,M_\odot$, following Munari et al. 2013). The MS is clearly elongated along the NE–SW direction. We used the moments of inertia method (Carter & Metcalfe 1980; Plionis & Basilakos 2002) to compute the ellipticity (ϵ) and orientation (PA).

Table 5
Results on the Detection of 3D Substructure in the Whole Sample of Cluster Members

Sub-clump	N_S	V	α(J2000)	δ(J2000)	ρ_S	χ^2_S
(1)	(2)	(3)	(4)		(5)	(6)
Hi-V	331	119907	04:16:10.2	−24:04:04	0.98	494
Lo-V	316	118201	04:16:05.4	−24:05:32	1.00	387
W	81	119136	04:15:32.9	−24:05:39	0.13	89
Sext	53	116900	04:16:18.8	−24:12:47	0.23	105

Note. Columns list the following information: (1) id of sub-clump, (2) number of assigned members, (3) peak velocity in km s^{-1}, (4) coordinates, (5) density relative to the densest peak, and (6) χ^2 value for each peak.

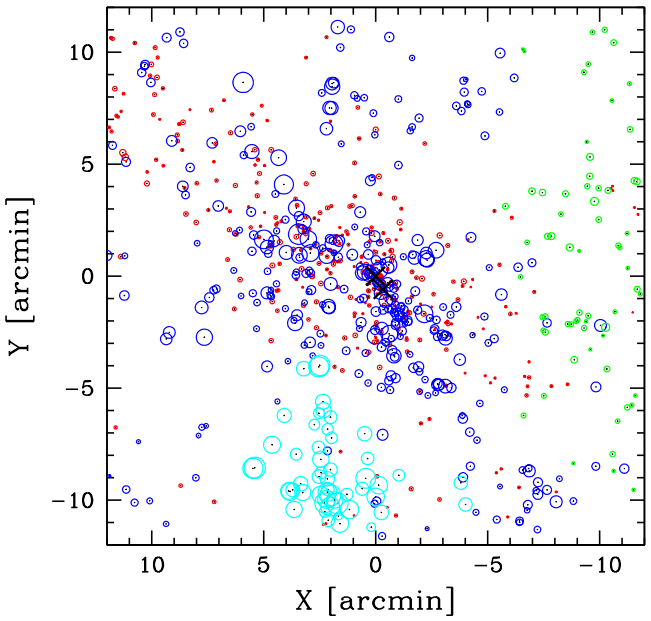

Figure 10. Spatial distribution of the 781 cluster member galaxies of the whole system. The sizes of the circles are weighted by the line-of-sight velocity of each galaxy. The positions of the two BCGs are marked with two black crosses. The four different colors indicate galaxies belonging to the four substructures detected through our 3D analysis, as described in the text: Lo-V (blue), Hi-V (red), W (green), and Sext (cyan).

We obtain $\epsilon = 0.31 \pm 0.03$ and PA $= 63° \pm 3°$ (measured counter-clock-wise starting from the north).

When looking at the spatial distribution of the two main subclusters on the plane of the sky (see Figure 8, lower panel), we find that galaxies belonging to the high-velocity subcluster (Hi-V) clearly concentrate around the central overdensity C, while those belonging to the low-velocity subcluster (Lo-V) are separated into two clumps centered on the secondary SW peak and the central overdensity C, being separated by ∼2′, which corresponds to ∼600 kpc and with a density ratio of 1:0.7. Thus, the central spatial overdensity C contains both low- and high-velocity galaxies.

The secondary SW peak is spatially coincident with a possible secondary mass concentration detected in the combined strong and weak gravitational lensing map by Jauzac et al. (2015), although we caution that, after careful re-analysis of combined SL and WL mass reconstruction using the Merten et al. (2009) model, we do not detect any lensing signal coincident with the SW galaxy overdensity (see Section 6 and Appendix). Given the absence of X-ray emission and their

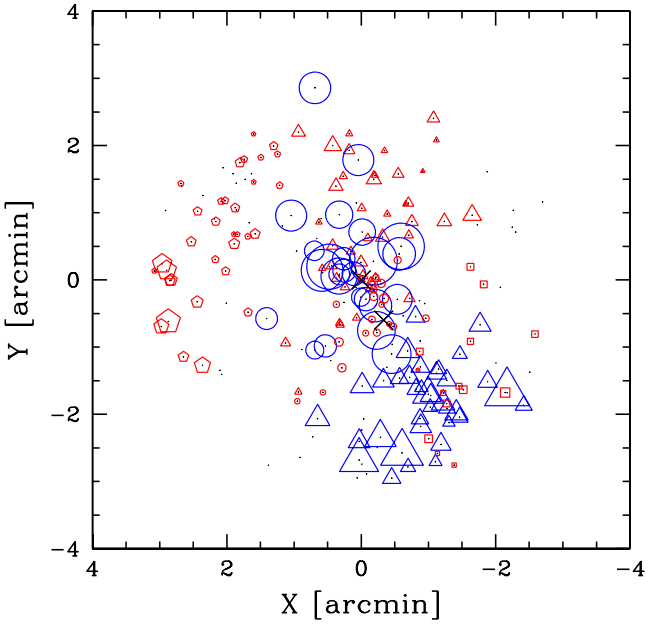

Figure 11. Same as Figure 10, but showing the results of the full 3D-DEDICA procedure applied to cluster member galaxies within 1 Mpc from the cluster center. Different symbols refer to the six groups detected through the full 3D-DEDICA analysis, as listed in Table 6: 1 (red triangles), 2 (blue triangles), 3 (red pentagons), 4 (blue circles), 5 (red circles), and 6 (red squares). Blue and red colors are assigned to groups having peak velocities close to the Lo-V and Hi-V subclusters, respectively. Blue circles and triangles highlight the complex 2D structure of the Lo-V subcluster.

lensing detection, Jauzac et al. (2015) concluded that this secondary SW clump is likely a non-virialized structure, possibly associated with a large-scale structure filament. However, the large number of spectroscopic redshifts has allowed us to find that the SW peak is, indeed, populated by a high concentration of low-velocity galaxies, comparable in number to the high-velocity galaxies around the C peak. Indeed, the analysis of deeper *Chandra* data by Ogrean et al. (2015) reveals the presence of X-ray emission out to the SW peak, where a discontinuity is detected in the density of the intra-cluster medium (ICM). Finally, we find no galaxy concentration around the secondary NE mass concentration reported by Jauzac et al. (2015).

We also used the full 3D-DEDICA procedure to analyze the cluster center, within a radius of 1 Mpc, a region encircling 223 cluster galaxies. The results of this analysis are shown in Figure 11 and Table 6. We detect six groups that are significant at $\gtrsim$99.99% c.l., having at least 10 galaxies, and with a relative density larger than 0.15. All of the groups have peak velocities that are very close to those of the Lo-V or Hi-V subclusters, supporting the fact that the structure of the cluster can be interpreted, as a first approximation, as bimodal. The peak velocities of the four groups related to the Hi-V subcluster lie in a small velocity range ($\Delta V_{\rm rf} < 300$ km s^{-1}). The two groups related to the Lo-V subcluster (group 2 and 4 in Figure 11 and Table 6) also have peak velocities that are not significantly separated according to both the 1D-DEDICA and 1D-KMM analyses. However, when analyzing the combined sample of 61 galaxies (36 plus 25 galaxies of group 2 and 4, respectively), the 2D-DEDICA method indicates a clear bimodality with two highly significant groups. This can also be clearly appreciated when looking at the distribution of blue circles and triangles in Figure 11. All of our analyses restricted to the central regions

Table 6
3D-DEDICA Results on Substructures within 1 Mpc from the Cluster Center

Sub-clump	N_S	V	α(J2000)	δ(J2000)	ρ_S	χ^2_S
(1)	(2)	(3)	(4)		(5)	(6)
1 Red Tria.	42	119725	04:16:08.9	−24:04:04	0.97	23
2 Blue Tria.	36	118189	04:16:05.0	−24:05:33	1.00	17
3 Red Pent.	33	120014	04:16:18.4	−24:03:07	0.30	13
4 Blue Circ.	25	118205	04:16:09.9	−24:03:55	0.44	8
5 Red Circ.	20	120159	04:16:08.4	−24:04:11	0.92	20
6 Red Squa.	13	119954	04:16:03.4	−24:05:39	0.15	6

Note. Columns list the following information: (1) id of sub-clump, (2) number of assigned members, (3) peak velocity in km s^{-1}, (4) coordinates, (5) density relative to the densest peak, (6) χ^2 value for each peak.

provide additional support in favor of the complex structure of the Lo-V subcluster.

According to the indicator test by Gebhardt & Beers (1991), the NE-BCG can be readily associated in velocity space with the Hi-V subcluster, and its projected position is coincident with the C peak spatial overdensity. The SW-BCG, however, has a >99% peculiar velocity with respect to the velocity distribution of galaxies of the Lo-V subcluster and it is spatially separated from both the SW and C overdensities (see Figure 8, lower panel). Interestingly, the SW-BCG seems to be unrelated to any galaxy concentration, although it is coincident with the position of the secondary peak of X-ray surface brightness (see Ogrean et al. 2015) and the SW mass halo detected via SL analysis by Grillo et al. (2015).

To conclude, MACS0416 is far more complex than a bimodal merging system with two spatially and dynamically separated galaxy clumps in 3D, each traced by a BCG. The observational picture points toward an atypical dynamical configuration of the cluster core composed of two main substructures, one of which shows a displacement of both its BCG and the hot, X-ray emitting gas with respect to the position of galaxies dynamically bound to the same substructure. We will discuss in Section 6 the possible scenarios that may lead to the observed spatial and dynamical configuration.

5. DYNAMICAL ANALYSIS: MASS PROFILES

In this section, we derive the mass profile of MACS0416 from the dynamical analysis of the spectroscopic sample of cluster members described in Section 3. We also provide a comparison between the mass profile derived from our dynamical analysis and those derived from strong lensing (Grillo et al. 2015), WL (Umetsu et al. 2014), and a combination of both (Umetsu et al. 2015), as well as those derived from X-ray data (see Appendix A; S. Ettori et al. 2016, in preparation).

As for the dynamical analysis presented in this paper, we constrain the mass profile using two different and complementary methods: the Modeling Anisotropy and Mass Profiles of Observed Spherical Systems (MAMPOSSt) by Mamon et al. (2013), and the so-called "Caustic technique" by Diaferio & Geller (1997).

The former method has been developed with the aim of breaking the degeneracy within the Jeans equation between the mass and the velocity anisotropy profiles. The code performs a maximum likelihood fit of the distribution of galaxies in the projected phase space in order to constrain the parameters that describe the profiles. On the one hand, the method assumes a

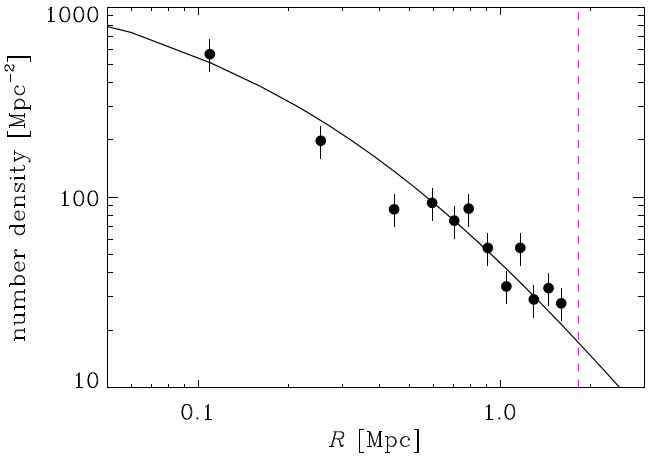

Figure 12. Projected galaxy number density profiles $n(R)$ (black dots with 1σ error bars) and best-fit projected NFW model (black solid line) for the whole galaxy cluster spectroscopic members. The vertical dashed line indicates the value of $r_{200} = 1.82$ Mpc, obtained from the weak-lensing analysis by Umetsu et al. (2014).

shape for the 3D velocity distribution, dynamical equilibrium of the cluster, and it requires parametrized models for the number density, the mass, and the velocity anisotropy profiles. On the other hand, MAMPOSSt requires no binning, differentiation, or extrapolation of the observables. Furthermore, MAMPOSSt does not assume any shape for the distribution function in terms of energy and angular momentum and it does not assume a Gaussian line-of-sight velocity distribution. Finally, any parametrization for the mass anisotropy and velocity profiles can be used with MAMPOSSt.

We consider the spectroscopic sample of cluster member galaxies obtained as described in Section 3. We first check the incompleteness of our spectroscopic sample, since this could affect the results of our dynamical analysis. In order to maximize completeness, we decided to restrict our analysis to the magnitude range $18 \leqslant Rc \leqslant 22.5$ and then to correct the sample of spectroscopic members for incompleteness as a function of magnitude. We also checked the completeness in radial bins from the cluster center and corrected for the spatial variation of completeness of our spectroscopic sample. However, we remark that in the magnitude range selected, spatial completeness is approximately constant (less than 10%–15% variation radially) from the cluster center out to the largest radii probed.

We proceed by fitting the scale radius parameter of a projected NFW (Navarro et al. 1997) density profile with a maximum likelihood technique. The best-fit value for the scale radius of the galaxy deprojected density profile is $r_\nu = 0.43 \pm 0.06$ Mpc. In Figure 12, we show the projected number density profile for the galaxy cluster spectroscopic members and the best-fit model.

We use the MAMPOSSt technique to calculate the best-fit values of the mass and anisotropy profile parameters. We restrict our analysis to the virial region where the cluster is more likely to have reached dynamical equilibrium. For the virial region, we use a region of radius $r_{200} = 1.82 \pm 0.11$ Mpc, as estimated from the WL by Umetsu et al. (2014).

In our analysis, we consider the Navarro et al. (NFW; 1997), Burkert (1995), Hernquist (1990), and Einasto (1965) mass profiles, which have been shown to provide good fits to many cluster mass profiles (Baes & Dejonghe 2002; Biviano et al. 2006; Rines & Diaferio 2006), and the Softened Isothermal

Table 7
Results of the Dynamical Analysis with MAMPOSSt

Model $M(r)$, $\beta(r)$ (1)	r_{200} (Mpc) (2)	r_s (Mpc) (3)	Vel. Anis. (4)	M_{200} ($10^{15}\,M_\odot$) (5)	Like Ratio (6)	$P(\chi^2)$ (7)
SIS, C	$1.72^{+0.09}_{-0.08}$	$0.02^{+0.05}_{-0.01}$	$1.12^{+0.46}_{-0.16}$	0.88 ± 0.13	1.00	...
Ein, C	$1.80^{+0.08}_{-0.10}$	$0.68^{+0.67}_{-0.20}$	$1.21^{+0.51}_{-0.16}$	1.01 ± 0.14	0.55	0.25
NFW, C	$1.80^{+0.08}_{-0.09}$	$0.63^{+0.57}_{-0.19}$	$1.23^{+0.52}_{-0.17}$	1.01 ± 0.14	0.51	0.28
Ein, T	$1.79^{+0.08}_{-0.11}$	$0.58^{+0.33}_{-0.13}$	$1.29^{+1.56}_{-0.29}$	0.99 ± 0.15	0.40	0.39
NFW, T	$1.78^{+0.08}_{-0.10}$	$0.53^{+0.29}_{-0.13}$	$1.28^{+1.52}_{-0.28}$	0.98 ± 0.15	0.37	0.42
Her, C	$1.83^{+0.08}_{-0.09}$	$1.50^{+1.07}_{-0.39}$	$1.28^{+0.53}_{-0.17}$	1.06 ± 0.15	0.36	0.43
Ein, O	$1.85^{+0.10}_{-0.11}$	$0.55^{+0.38}_{-0.14}$	$0.91^{+0.86}_{-0.14}$	1.10 ± 0.18	0.30	0.51
NFW, O	$1.83^{+0.12}_{-0.10}$	$0.46^{+0.30}_{-0.11}$	$0.98^{+1.02}_{-0.21}$	1.05 ± 0.19	0.27	0.54
Bur, C	$1.83^{+0.08}_{-0.07}$	$0.36^{+0.20}_{-0.09}$	$1.31^{+0.57}_{-0.19}$	1.06 ± 0.13	0.21	0.63
Her, T	$1.81^{+0.07}_{-0.09}$	$1.23^{+0.54}_{-0.24}$	$1.35^{+1.70}_{-0.30}$	1.03 ± 0.14	0.21	0.63
Her, O	1.89 ± 0.11	$1.18^{+0.68}_{-0.29}$	$0.84^{+0.73}_{-0.11}$	1.17 ± 0.20	0.15	0.71
Bur, T	$1.80^{+0.07}_{-0.08}$	$0.29^{+0.12}_{-0.06}$	$1.29^{+1.50}_{-0.27}$	1.02 ± 0.12	0.11	0.78
Bur, O	1.83 ± 0.08	$0.25^{+0.07}_{-0.05}$	$0.97^{+0.95}_{-0.19}$	1.06 ± 0.15	0.07	0.84

Note. Columns list the following information: (1) model used for the mass profile, $M(r)$, and recipe used for the velocity anisotropies, $\beta(r)$, (2) r_{200}, (3) scale radius r_s, (4) derived velocity anisotropy, σ_r/σ_θ, where $\beta = 1 - (\sigma_\theta/\sigma_r)^2$, constant with radius for the C model and evaluated at radius ∞ for the O and T models, (5) mass within r_{200}, (6) likelihood ratios relative to the best-fit model, and (7) χ^2 probability, as obtained using the likelihood-ratio test, that the considered model is a worse representation of the data compared to the best-fit model (SIS+C). The uncertainties listed in this table refer to the 1σ marginalized errors on each of the free parameters in our MAMPOSSt analysis. The scale radius is r_{-2} for the NFW and Einasto models, $r_H = 2r_{-2}$, $r_B \simeq 2/3r_{-2}$, and the core radius, for the Hernquist, Burkert, and SIS $M(r)$ models, respectively.

Sphere (SIS; Geller et al. 1999). All of these models, except the Einasto (1965) model, have two free parameters: the virial radius r_{200} and a scale radius r_s, which corresponds to the radius r_{-2} for the NFW and Einasto (1965) models, where the logarithmic derivative of the mass density profile is $d\ln\rho/d\ln r = -2$. We fix the additional free parameter in the Einasto (1965) model to $m = 5$, as in Biviano et al. (2013).

As for the velocity anisotropy profile, following Biviano et al. (2013), we consider three models:

1. "C": constant anisotropy with radius, $\beta = \beta_C$;
2. "T": anisotropy profile from Tiret et al. (2007);
3. "O": anisotropy of opposite sign at the center and at large radii.

The "C" model depends only on one parameter: the constant value of the velocity anisotropy β_C. The "T" and "O" models depend, instead, on two parameters: a scale radius, r_β, and the anisotropy at a large radius, β_∞. We fix $r_\beta \equiv r_{-2}$ in our models.

We consider only the "C" model in combination with the SIS mass profile because r_{-2} cannot be uniquely defined for the SIS mass profile model. Therefore, we run MAMPOSSt on 13 combinations of mass and velocity-anisotropy profile models, with three free parameters: the virial radius r_{200}, the scale radius r_s of the mass profile, and β_∞ or β_C. We use the optimization routine NEWUOA (Powell 2004) to find the maximum likelihood solutions.

The best-fit values of these parameters are presented in Table 7 along with their marginalized errors obtained by integrating the posterior probabilities over the other parameters. We find that the best-fit model is obtained for a combination of an SIS mass profile and a "C" velocity anisotropy profile. Other combinations of models are statistically acceptable (at the 1σ level) according to the likelihood-ratio test by Meyer (1975). These are the models listed in Table 7. The probability values of this test are listed in the last column of Table 7. We also list the values of the likelihood ratios relative to the best-fit model.

The best-fit mass profile model for MACS0416 is the SIS model. This model has been shown to provide unacceptable fits to the mass profiles of clusters from the CAIRNS (Cluster and Infall Region Nearby Survey; Rines et al. 2003) and ENACS (ESO Nearby Abell Cluster Survey; Katgert et al. 2004) surveys. Most likely, the mass profile of MACS0416 is different from the average cluster mass profile because it is clearly not a dynamically relaxed cluster. Remember that MAMPOSSt assumes dynamical relaxation, which might not be appropriate in the case of MACS0416. However, as shown in Figure 13, despite the dynamically complex and clearly unrelaxed status of the cluster, especially in the core region, the best-fit mass profile found by MAMPOSSt is in relatively good agreement with the mass profiles obtained from all other independent probes and mostly within the 1σ uncertainties. More specifically, in Figure 13, for comparison, we plot the mass profile reconstruction from the SL analysis by Grillo et al. (2015), a combination of the WL reconstruction by Umetsu et al. (2014) and the SL model by Grillo et al. (2015), and the mass profile reconstructed from the X-ray data. The X-ray mass profile has been obtained under the assumption of a spherically symmetric ICM in hydrostatic equilibrium with the underlying gravitational potential, which also might not be appropriate for an unrelaxed cluster. A brief description of the method used to obtain the X-ray mass profile can be found in the Appendix. We note that the largest deviations are found between the dynamical profile and the X-ray profile around ~300–400 kpc from the cluster center. These deviations are most likely due to the presence of the secondary peak of X-ray emission associated with the SW-BCG, which was not removed in the measurement of the hydrostatic X-ray mass presented here. Given the high X-ray temperature, it is not possible to mask this secondary peak without a loss of information. We are

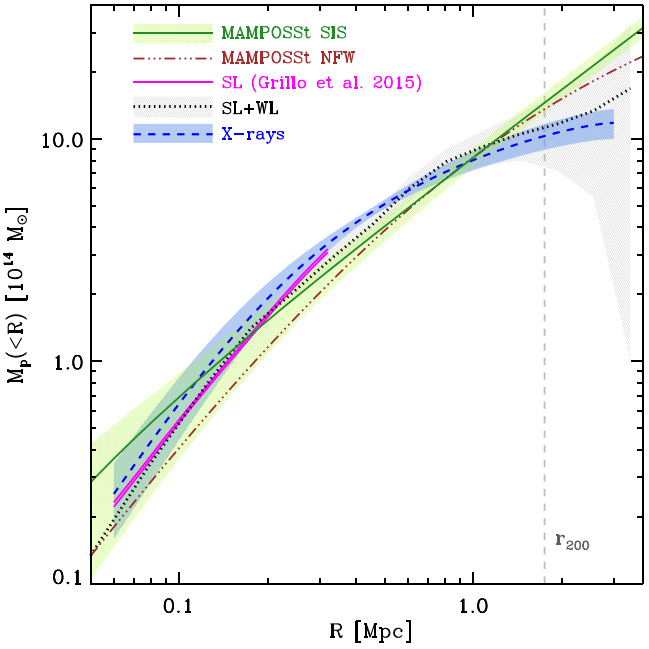

Figure 13. Projected cumulative mass profile $M_p(<R)$ with 1σ confidence intervals for the MAMPOSSt projected SIS solution (green solid line and hatched region) and for the projected NFW solution (brown dash-triple-dotted line), both derived from a simple spherical component. For comparison, we plot the high-precision SL mass reconstruction by Grillo et al. (2015; magenta solid lines) and its combination with the weak-lensing reconstruction by Umetsu et al. (2014; black dotted line and gray hatched region), as well as the mass profile from our X-ray analysis (blue dashed line and hatched region). The dashed vertical line indicates the value of r_{200} obtained from our dynamical analysis with the SIS model. The position of the NE-BCG (R.A. = 04:16:09.14, decl. = −24:04:03.1) has been adopted as the center of the cluster for all of the different profile reconstructions plotted here.

currently working on a reconstruction of the X-ray mass which includes a reliable modeling of this secondary X-ray halo. Also, remember that throughout our analysis, the cluster center has been fixed on the NE-BCG, which marks the location of the bottom of the potential well of the system as shown by the SL mass reconstruction (Grillo et al. 2015). This is true for all of the different probes of the mass profiles shown in Figure 13. In particular, the mass reconstructions from SL and WL are slightly different from those previously published because of the slightly different choice of the center.

The relatively good agreement among the mass profiles obtained from different probes, especially around the virial radius, leads to a good match between estimates of the cluster virial mass from different probes: for instance, when comparing the deprojected values, the best-fit SIS model of MAMPOSSt yields a virial mass of $M_{200,c} = 8.8 \pm 1.3 \times 10^{14} M_{\odot}$, which is consistent within the uncertainties with the value obtained through the present SL+WL analysis, $M_{200,c} = 11.2 \pm 2.6 \times 10^{14} M_{\odot}$ ($M_{200,c} = 10.7 \pm 2.6 \times 10^{14} M_{\odot}$ in the SL+WL analysis presented in Umetsu et al. 2015).

In order to extend the determination of the cluster mass profile beyond the virial region, we use the Caustic technique. This technique aims to identify density discontinuities in the distribution of galaxies in the plane of the rest-frame, line-of-sight velocity versus projected radii. Discontinuities are identified using, not only cluster members, but all of the galaxies of the sample. The Caustic technique offers the advantage of allowing us to calculate the mass of a cluster without assuming any parametrization for the profile and without the assumption of dynamical equilibrium. Following Diaferio (1999), one has to solve the following equation:

$$M(<r) - M(<r_{\rm min}) = \frac{1}{G}\int_{r_{\rm min}}^{r} A^2(x) F_\beta(x) dx, \qquad (1)$$

where A is the amplitude of the Caustic curve that is directly related to the cluster potential, G is the gravitational constant, and F_β is

$$F_\beta(r) = -2\pi G \frac{\rho(r) r^2}{\phi(r)} \frac{3 - 2\beta(r)}{1 - \beta(r)}, \qquad (2)$$

where $\rho(r)$ is the cluster mass density profile and $\phi(r)$ is the gravitational potential of the cluster.

We first determine the amplitude A. In Figure 6, we show the isodensity curves in the rest-frame line-of-sight velocity versus projected radius plane, computed using a Gaussian adaptive kernel with an "optimal" kernel size, following Silverman (1986). Although theory defines the Caustic as the curve of infinite density, in practice, we proceed following Diaferio (1999). We use the determination of r_{200} from the lensing analysis of Umetsu et al. (2014). We select all of the galaxies with a rest-frame velocity $-6000 \leqslant V_{\rm rf} \leqslant 6000\,{\rm km\,s^{-1}}$ and we mirror the data with respect to the y axis (at $R = 0$ Mpc). This last step is necessary to suppress any edge-effect. Then, we calculate the isodensity profile and, finally, we define the Caustic as the curve which, within r_{200}, minimizes $|\langle v({\rm esc}, R)^2\rangle - 4\sigma_v^2|$, where $\langle v({\rm esc}, R)^2\rangle$ is the mean square escape speed determined from the Caustic amplitude within R, and σ_v is the velocity dispersion of the member galaxies. Then, we symmetrize the Caustic with respect to the zero-velocity axis by choosing, in each radial bin, the smaller absolute value of the Caustics among the two positive and negative velocities.

Once we have obtained the amplitude of the Caustic, A, we calculate the normalization F_β. The weakness of the Caustic method is that it needs to assume a value of F_β, which generally comes from simulations, while its strength is that it can be used beyond the virial radius. Since the mass profile of MACS0416 within the virial radius has already been reconstructed using different methods, we use the Caustic method to probe the mass profile at larger cluster-centric distances.

In particular, we can determine the value of F_β. This can be obtained by requiring that the Caustic-derived mass value between $R = 0$ and $R = r_{200}$ equals the value obtained with MAMPOSSt (this technique was first described and applied to the cluster MACS J1206.2-0847 in Biviano et al. 2013). For MACS0416, we find $F_\beta = 0.55$, which is in good agreement with the results of Diaferio & Geller (1997) and Diaferio (1999), while the most recent implementations of the caustic algorithm by Serra et al. (2011) and Gifford et al. (2013) favor a slightly higher value ($F_\beta = 0.68$). On the other hand, a value as low as 0.5 has still been used recently by Geller et al. (2013). It is possible that there is a real cluster-to-cluster variance in the value of F_β, which is probably related to an intrinsic variance in the shape of the different cluster mass profiles. Hydrodynamical simulations have shown that the scatter on F_β is large (see Figure 4 of Serra et al. 2011). We also stress that given the unrelaxed nature of MACS0416 and the assumptions of spherical symmetry and dynamical equilibrium in the MAMPOSSt mass profile reconstruction, our determination of F_β may be affected by systematics in this particular cluster.

Once we have determined A and F_β, we can use the Caustic method to extend the mass profile reconstruction beyond r_{200}.

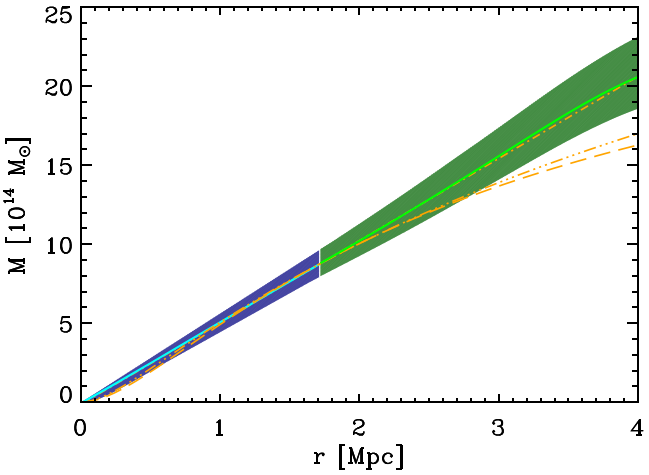

Figure 14. Mass profile of MACS0416 (with 1σ uncertainties) as obtained from the dynamical analysis. The MAMPOSSt best-fit solution (SIS) and its 1σ error are represented by the cyan solid curve and blue region. The MAMPOSSt best-fit solution is also shown extended beyond r_{200} (yellow dashed–dotted line). The Caustic profile and its 1σ error are represented by the green solid line and the green region. For comparison, we also show NFW (three dotted–dashed orange line) and Hernquist (long dashed orange line) profiles with the same r_{200} as the MAMPOSSt best-fit solution and r_s as given in Table 7.

The uncertainties on this profile are obtained by convolving the error on the measurement of M_{200} obtained from MAMPOSSt with the error on the Caustic $M(<r)$, as described in Diaferio (1999), but multiplied by a factor 1.4 to have $\sim 1\sigma$ errors (in fact, the original prescription by Diaferio 1999 led to estimated 50% confidence levels, see Serra et al. 2011).

The final mass profile obtained from the dynamical analysis, resulting from the combination of the MAMPOSSt and Caustic techniques, is shown in Figure 14. In this plot, we also compare our mass profile reconstruction with the NFW, Hernquist, and SIS models, all using the same value of $r_{\rm vir} = 1.77$ Mpc (the best-fit MAMPOSSt solution for the SIS model) and the values of r_s listed in Table 7. This plot shows how, at large radii, the mass profile of MACS0416 is still well described by a SIS model, while it significantly deviates from the NFW or Hernquist model.

6. DISCUSSION

The offset between the collisional (hot gas) and non-collisional (stars and dark matter) mass components in merging galaxy clusters can be used to constrain the dark matter cross-section (e.g., Markevitch et al. 2004; Harvey et al. 2015) as well as the dynamical configuration of the merger. A significant offset between the hot, X-ray emitting gas and dark matter, generally traced by lensing, is a clear signature of a post-merging scenario, while no offset between the two mass components suggests either a pre-merging phase or a configuration aligned along the line of sight. Recent results from deeper *Chandra* data of MACS0416 showed that both of the detected X-ray peaks (NE and SW) have very small displacement (a few arcsec in projection) with respect to the position of the two extended dark matter halos detected through gravitational lensing (see Ogrean et al. 2015). We verified that this is also true when adopting the more recent, high-precision, SL mass reconstruction by Grillo et al. (2015), as shown in Figure 15. Although the small offset seems to support a pre-merging scenario, it could still be consistent with a post-merger phase if the merging of the two main subclusters occurred along the line of sight.

From our dynamical and structural analysis, we find that galaxies belonging to the NE and SW subclusters, as well as the two BCGs, are well separated in the projected velocity space (as clearly shown in Figure 7) with a difference in projected line-of-sight velocities of the order of 900 km s^{-1}, where the NE subcluster has higher velocity than the SW one. This, together with the lack of a significant offset between dark matter and hot gas, could suggest that the merger is oriented along the line of sight. However, there are at least two additional complications in this scenario: (1) the low-velocity subcluster (Low-V) is split into two distinct, well-separated ($\sim$600 kpc) sub clumps (C and SW) and (2) the SW-BCG is isolated, i.e., offset from any galaxy concentration.

We now discuss possible interpretations to reconcile the X-ray results (Ogrean et al. 2015) with those of our structural analysis in a consistent picture.

The X-ray temperature of the hot ICM of this massive cluster is high ($\sim$10 keV), with no evidence of a cooling core and a very high value of the central entropy (Donahue et al. 2014). This is expected in merging clusters, since the central hot gas has been shock-heated and has not yet had enough time to cool.

The sound speed in a cluster with a temperature of $\sim$10 keV is $\sim$1300 km s^{-1}, while typical collision velocities are 1–2 times the sound speed. The observed projected velocity difference between the two BCGs ($\Delta V_{\rm rf} \sim 900$ km s^{-1}), as well as the projected velocity difference between the two main subclusters ($\Delta V_{\rm rf} \sim 1200$ km s^{-1}), together with evidence that the merging is very likely happening at an intermediate angle between the LOS and the plane of the sky, imply that the collisional velocity could well be close to or above supersonic. The absence of a cool component in the X-ray gas around the cluster core (corresponding to the X-ray emissivity peak and the projected C galaxy overdensity) seems to suggest that the cluster core must have already experienced some perturbation. We also note that the X-ray surface brightness presents at least two density discontinuities in the SW direction toward the secondary X-ray emission peak: the first one around the SW-BCG and the second one toward the SW galaxy overdensity (see Ogrean et al. 2015).

Together with the absence of a cool gas component, the presence of an X-ray cavity around the NE-BCG with no associated radio emission provides an additional important clue. In a post-merging scenario, a cavity could have had enough time to form since first core passage. However, given the short timescale and the intense turbulence following the first core passage, forming a new cavity would have required a strong active galactic nucleus (AGN) outburst and the right timing. The expectation would be to observe radio emission associated with the X-ray cavity, but this is not observed. Instead, the presence of the X-ray cavity itself supports a pre-merger scenario. The cavity was most likely inflated by a recent weak outburst of the AGN in the NE-BCG.

As shown by Ogrean et al. (2015), the diffuse radio emission detected both in the JVLA and GMRT data extends to a size of $\sim$0.6 Mpc, which is smaller than that of the typical radio halos in merging clusters (1–1.5 Mpc; e.g., Feretti et al. 2012). The size of the radio halo in MACS0416 is more similar to that of radio mini-halos typically found in cool-core clusters (e.g., Giacintucci et al. 2014), but no evidence of a cool core is found from the X-rays. The radio halo seems to be associated with

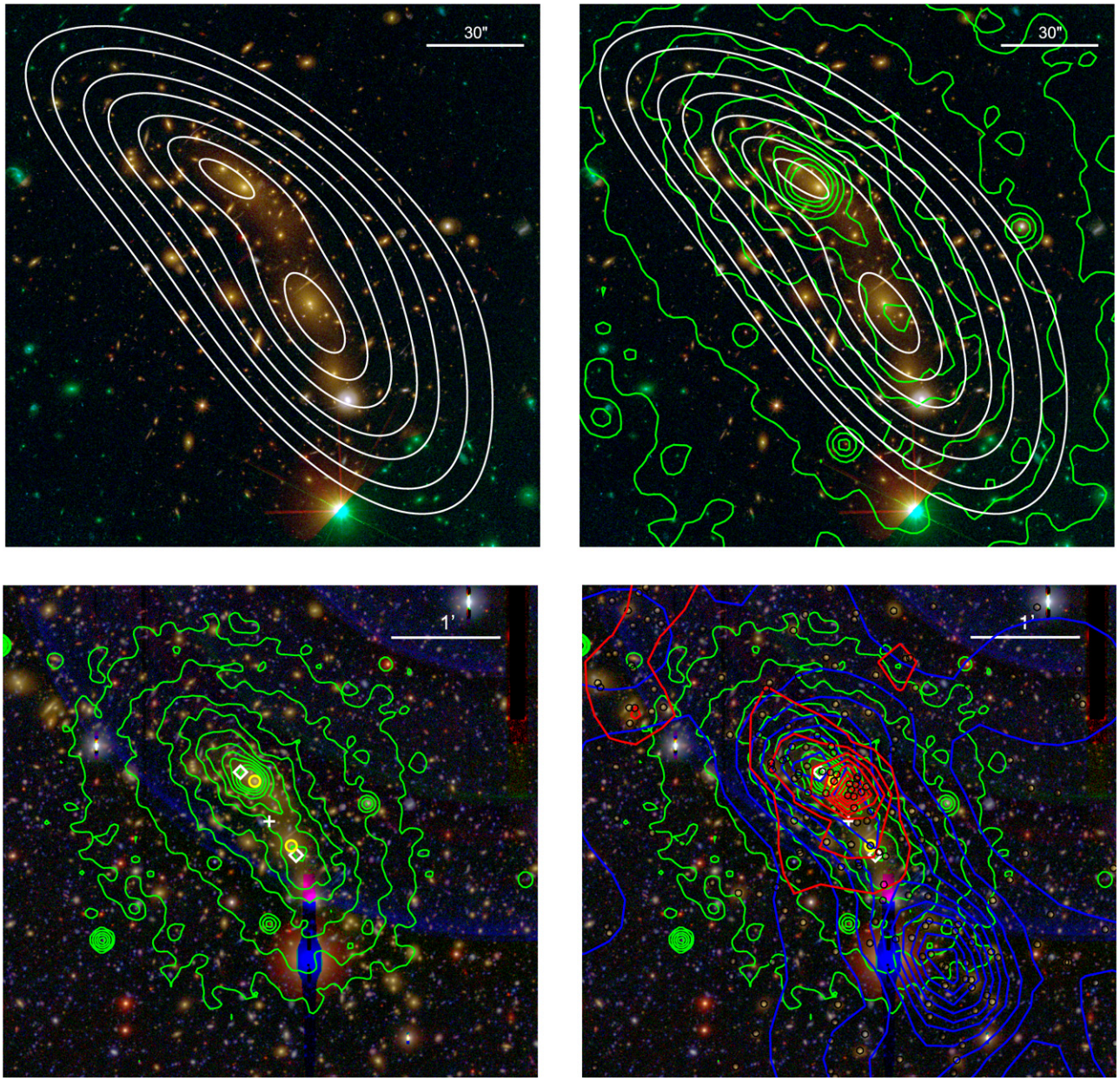

Figure 15. Top left: *HST* color image with extended mass halo from SL modeling (white, Grillo et al. 2015) contours overlaid. Top right: same as the top left figure, but with the addition of 0.5–2 keV X-ray (green, Ogrean et al. 2015) contours overlaid. Bottom left: Subaru color image with X-ray contours overlaid (green). The positions of the two extended dark matter halos (white diamonds) and the barycenter (white cross) calculated by Grillo et al. (2015) are marked. The positions of the two BCGs are indicated with two yellow circles. Bottom right: same as in the bottom left figure, but with the galaxy 2D-isodensity contours of the two main subclusters from our 3D analysis overlaid. Blue and red isodensity contours are for galaxies of the low- (Lo-V) and high-velocity (Hi-V) subclusters, respectively. Black circles mark cluster member galaxies of our spectroscopic sample.

both subclusters. It could be a single halo originating from the main merger event or it could be a superposition of two individual halos where each of the two halos must have been generated by previous merger events within the two subclusters themselves.

Indeed, another possible scenario could be that multiple mergers occurred over the past ∼1 Gyr, which is also postulated by numerical simulations (Poole et al. 2008). In this case, while the cluster core would have already relaxed back to a compact state, it should not have had enough time to cool back again. Some cool gas is expected to survive the merger, but it could be difficult to detect given the different, unknown emission measure of the cold and hot ICM components, which in this case are probably overlapping in projection.

The dynamics of the galaxies belonging to the two main merging subclusters is complex. The velocity and spatial distribution of galaxies is not the typical bimodal distribution observed in merging clusters. We find a clear spatial displacement between the SW-BCG and the bulk of the Lo-V subcluster to which it seems to be dynamically bound. As our 3D analysis has shown, the Lo-V subcluster is highly substructured, being composed of two spatial overdensities of galaxies (separated by ∼600 kpc) and an isolated BCG sitting halfway between the central overdensity and the SW subclump. A possible scenario capable of explaining the observed

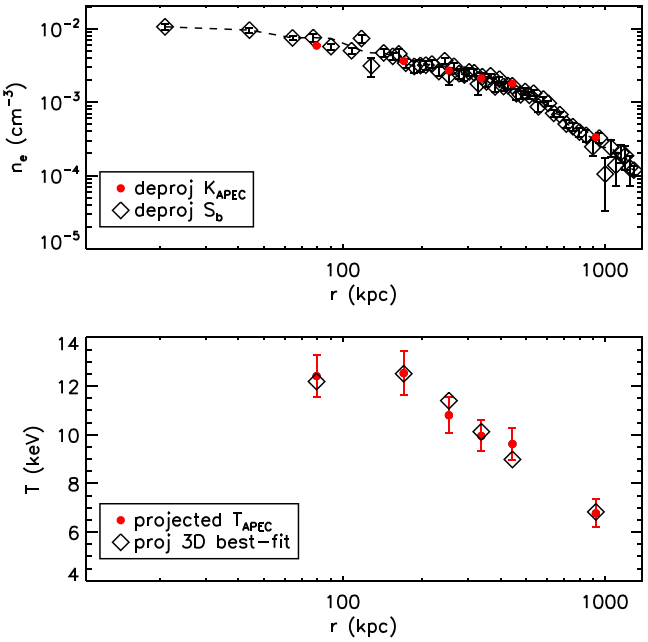

Figure 16. Top panel: electron density profiles obtained from both the geometrically deprojected surface brightness profile (black diamonds) and the normalization of the thermal component fitted to the extracted spectra (red circles). Bottom panel: best-fit spectral measurements of the gas temperature (red circles). The black diamonds represent the projection in the spectral bins of the best-fit 3D temperature profile obtained by inverting the hydrostatic equilibrium equation in combination with the deprojected surface brightness profile (black diamonds in the top panel).

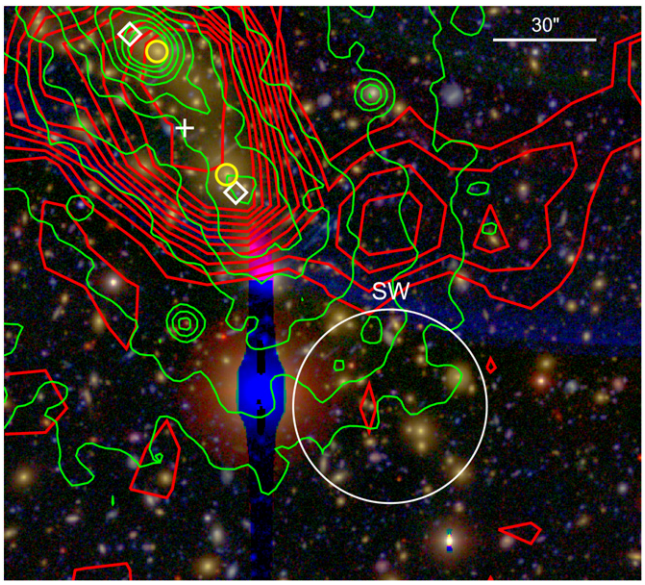

Figure 17. Subaru color image with overlayed convergence contours (red) obtained from the combined SL and WL model described in the text. X-ray contours are also displayed in green. The positions of the two extended dark matter halos (white diamonds) and the barycenter (white cross) calculated by Grillo et al. (2015) are marked. The positions of the two BCGs are indicated with two yellow circles. The position of the SW overdensity of cluster member galaxies is indicated with a white circle.

complex spatial and dynamical configuration, as well as the possible X-ray density discontinuity observed toward the SW sub-clump (see Ogrean et al. 2015), would be the following: the Lo-V subcluster could be itself the result of a previous or ongoing merger occurring at an angle close to the plane of the sky, while the two main subclusters (Lo-V and Hi-V) are most likely in a pre-merging phase. Although to a lesser extent, the NE part of the cluster could also have been affected by some merging, given the small concentration of galaxies detected at NE in the Hi-V subcluster (see Figure 8).

In order to assess the significance of the detection of the SW galaxy overdensity in the lensing shear signal, we analyzed a lensing mass reconstruction obtained using a multi-scale grid lensing model that combines WL and SL reconstruction following the methodology of Merten et al. (2009). The surface-mass–density contours obtained with this model show no significant overdensity around the relevant cluster members galaxies, indicating that the projected mass of the SW sub-clump must be significantly smaller than previously estimated by Jauzac et al. (2015). The results obtained with this lensing analysis and some additional checks on their robustness are provided in the Appendix.

In conclusion, the complex structure we detect in the core of MACS0416 is consistent with a scenario in which the two main subclusters are in a pre-merging phase, although each subcluster could be the result of a recent merger, which would be more dramatic in the Lo-V subcluster. Recent hydrodynamical modeling of the gas and dark matter by Diego et al. (2015) supports our pre-merger conclusion, demonstrating that relatively small offsets between gas and dark matter are expected at the early stage of the encounter due to gas compression when the separation of the two main components is less than the combined sum of their virial radii. The displacement of the SW-BCG could be explained by dynamical friction or by a close encounter and tidal interaction with some other massive galaxy in the cluster core. An analogous example of a displaced, isolated BCG is that of the Coma cluster (see Biviano et al. 1996; Neumann et al. 2003). Note also that the ICL, clearly detected in both ground-based and *HST* images, is elongated approximately along the line connecting the two BCGs and closely following the elongation of the X-ray emission (see Figure 15).

Given the unrelaxed dynamical state of the cluster core, it is worth briefly discussing the results of our dynamical analysis. We have shown that for this complex merging cluster, the mass profile is best described by an SIS model, rather than by an NFW profile. This may point toward interesting deviations from universality during the major-merger phases in the cluster assembly history. However, one cluster is certainly not sufficient for us to derive solid conclusions on the effect of mergers on the total mass profile, as well as on the biases affecting different mass probes. We defer further investigation of the unrelaxed clusters of our CLASH-VLT sample and comparison with hydrodynamical simulations to a future work.

Further refinement of the dynamical analysis presented in this work, in particular, by abandoning a single spherical component approximation and *thus reducing systematics*, is underway and will be presented in a future publication (B. Sartoris et al. 2016, in preparation).

7. CONCLUSIONS

We performed a detailed dynamical and structural analysis of the Frontier Fields cluster MACS0416 based on 781 spectroscopically confirmed cluster members.

Our analysis shows that the cluster structure is more complex than that of a bimodal merger. The most likely emerging

Table 8
Redshifts of X-Ray Sources in the Field of MACS0416

ID	R.A.	decl.	z	QF	Ref.	Mag
(1)	(2)	(3)	(4)	(5)	(6)	(7)
Chandra Sources						
CLASHVLTJ041524.4-240449	63.851613	−24.080402	0.3150	3	1	19.49
CLASHVLTJ041529.3-240620	63.871900	−24.105615	0.6399	3	1	22.32
CLASHVLTJ041532.1-240259	63.883668	−24.049812	2.0723	3	1	21.13
CLASHVLTJ041536.6-240648	63.902366	−24.113490	0.3547	3	1	19.95
CLASHVLTJ041538.6-235438	63.910659	−23.910696	2.3129	3	1	18.92
CLASHVLTJ041539.5-240232	63.914738	−24.042268	0.3984	3	1	22.51
CLASHVLTJ041542.5-240126	63.927177	−24.023894	0.4015	3	1	21.07
CLASHVLTJ041546.2-235727	63.942583	−23.957776	1.6857	3	1	19.50
CLASHVLTJ041547.7-241121	63.948598	−24.189198	0.3037	3	1	20.48
CLASHVLTJ041551.2-240957	63.963448	−24.165885	0.5691	2	1	22.01
CLASHVLTJ041552.0-235702	63.966847	−23.950565	1.4959	3	1	22.51
CLASHVLTJ041553.2-235811	63.971504	−23.969948	1.9899	3	1	23.33
CLASHVLTJ041553.7-240815	63.973841	−24.137775	2.4928	3	1	22.50
CLASHVLTJ041554.7-235706	63.978027	−23.951751	0.3075	3	1	19.26
CLASHVLTJ041556.0-241509	63.983157	−24.252706	0.4193	3	2	20.43
CLASHVLTJ041557.1-240425	63.987727	−24.073615	0.0000	3	1	15.28
CLASHVLTJ041557.3-235639	63.988751	−23.944318	2.9691	3	1	21.23
CLASHVLTJ041559.1-240320	63.996110	−24.055575	0.3903	3	1	20.18
CLASHVLTJ041559.9-240517	63.999418	−24.088297	0.5690	3	1	22.65
CLASHVLTJ041600.4-235721	64.001827	−23.955929	1.0167	3	1	20.67
CLASHVLTJ041600.4-241330	64.001638	−24.225091	0.3439	3	1	20.05
CLASHVLTJ041600.7-240010	64.002833	−24.002840	1.4572	3	1	19.48
CLASHVLTJ041603.7-235516	64.015484	−23.921314	1.7844	3	1	21.26
CLASHVLTJ041604.6-240414	64.019065	−24.070821	0.4111	3	1	19.24
CLASHVLTJ041606.2-241328	64.026017	−24.224534	0.5697	3	3	22.13
CLASHVLTJ041606.9-240120	64.028810	−24.022490	2.1517	9	1	24.27
CLASHVLTJ041607.5-240730	64.031228	−24.125260	0.3550	3	2	19.58
CLASHVLTJ041608.0-240920	64.033244	−24.155826	2.1311	3	1	21.87
CLASHVLTJ041608.4-235949	64.034888	−23.997007	0.3068	3	1	23.49
CLASHVLTJ041608.8-240925	64.036819	−24.157175	2.1915	3	3	23.87
CLASHVLTJ041609.8-240051	64.041017	−24.014281	0.5605	9	1	24.05
CLASHVLTJ041611.4-240024	64.047656	−24.006897	0.1535	3	1	18.03
CLASHVLTJ041613.3-241206	64.055284	−24.201708	1.3670	2	2	21.68
CLASHVLTJ041613.5-240822	64.056455	−24.139513	2.0760	3	1	22.05
CLASHVLTJ041613.9-240510	64.057793	−24.086357	0.4992	6	5	20.75
CLASHVLTJ041614.5-240047	64.060523	−24.013144	0.3520	3	3	20.21
CLASHVLTJ041615.3-240530	64.063601	−24.091894	2.2072	3	1	23.74
CLASHVLTJ041616.3-235917	64.067802	−23.988083	0.4627	2	1	22.17
CLASHVLTJ041618.2-235632	64.075664	−23.942274	0.3906	3	1	21.04
CLASHVLTJ041619.5-240247	64.081083	−24.046522	0.3955	3	1	19.43
CLASHVLTJ041620.1-241007	64.083577	−24.168858	1.3647	3	1	23.16
CLASHVLTJ041620.7-240511	64.086382	−24.086521	0.3991	5	4	20.09
CLASHVLTJ041623.3-240408	64.097065	−24.069136	2.1201	3	1	22.90
CLASHVLTJ041623.3-240613	64.096987	−24.103652	2.4718	3	1	22.96
CLASHVLTJ041624.3-240845	64.101395	−24.145976	0.2677	3	3	20.33
CLASHVLTJ041624.8-240753	64.103322	−24.131653	1.6901	3	1	19.65
CLASHVLTJ041627.2-240854	64.113505	−24.148384	0.4661	3	1	20.30
CLASHVLTJ041627.9-240032	64.116082	−24.009063	1.9569	3	1	20.21
CLASHVLTJ041629.2-240213	64.121604	−24.036946	4.1494	3	1	19.69
CLASHVLTJ041630.2-235742	64.125989	−23.961766	1.1927	3	1	19.67
CLASHVLTJ041630.4-240532	64.126515	−24.092477	0.3380	3	1	20.28
CLASHVLTJ041632.0-240618	64.133494	−24.105221	0.7110	3	1	22.48
CLASHVLTJ041638.8-235942	64.161665	−23.995040	2.3779	3	1	23.47
CLASHVLTJ041639.2-240319	64.163437	−24.055474	0.6332	3	2	24.52
CLASHVLTJ041639.9-240207	64.166129	−24.035398	2.1216	3	1	21.15
CLASHVLTJ041640.2-235814	64.167684	−23.970560	0.6217	3	1	22.32
CLASHVLTJ041648.8-240243	64.203525	−24.045421	1.1785	3	1	21.93
CLASHVLTJ041654.3-240754	64.226124	−24.131936	0.5882	3	2	21.94
CLASHVLTJ041700.6-240350	64.252481	−24.064163	0.3009	3	1	19.65
CLASHVLTJ041705.1-240049	64.271075	−24.013635	0.5531	3	1	19.70
Serendipitous AGN						
CLASHVLTJ041529.6-235538	63.873166	−23.927416	3.6528	3	1	21.84

Table 8
(Continued)

ID (1)	R.A. (2)	decl. (3)	z (4)	QF (5)	Ref. (6)	Mag (7)
CLASHVLTJ041541.7-235916	63.923836	−23.988006	0.3559	3	1	22.46
CLASHVLTJ041544.9-240733	63.937133	−24.125920	3.0600	3	1	22.94
CLASHVLTJ041605.6-241158	64.023505	−24.199521	0.4497	3	1	22.65
CLASHVLTJ041619.9-241150	64.082823	−24.197260	2.4718	3	1	24.10

Note. Columns list the following information: (1) VIMOS identification number, (2–3) coordinates, (4) spectroscopic redshift, (5) redshift quality flag, (6) reference (i.e., CLASH-VLT VIMOS: 1—based on LR-Blue spectra, 2—based on MR spectra, 3—based on a combination of LR-Blue and MR spectra, 4—Ebeling et al. (2014), 5—*Magellan*, (D. Kelson 2016, private communication)), and (7) Subaru R-band magnitude.

(This table is available in machine-readable form.)

scenario is that where the two main subclusters are seen in a pre-merging phase, although each subcluster could be the result of a recent merger, which is more evident in the Lo-V subcluster. The displacement of the SW-BCG could be explained by dynamical friction or by a close encounter and tidal interaction with some other massive galaxy in the cluster core.

The cluster mass profile reconstructed through our dynamical analysis is best fit by an SIS model, significantly deviating from a NFW profile, especially at large radii (beyond the virial radius). Despite the complex and clearly unrelaxed nature of this massive cluster, the mass profile reconstruction obtained through our dynamical analysis is in good agreement with those obtained from strong and WL, as well as with that from the X-rays.

Separate studies focused on the influence of the environment on different galaxy populations and their interplay with the substructures of this cluster will be presented in subsequent papers (Maier et al. 2016, A. Mercurio et al. 2016, in preparation).

We thank the anonymous referee for a careful reading of the manuscript and the valuable comments and suggestions provided. We acknowledge the continuous help of the ESO user support group, especially our project support astronomer, Vincenzo Mainieri, for his excellent support and advices. We acknowledge financial support from PRIN-INAF 2014 1.05.01.94.02 and from MIUR PRIN2010-2011 (J91J12000450001). I.B. acknowledges funding support from the European Union Seventh Framework Programme (FP7/2007-2013) under grant agreement No. 267251 "Astronomy Fellowships in Italy" (AstroFIt). B.S. acknowledges a grant from "Consorzio per la Fisica—Trieste." P.R. acknowledges the hospitality and support of the visitor program of the DFG cluster of excellence "Origin and Structure of the Universe." G.A.O. and A.Z. are supported by NASA through Hubble Fellowship grants HST-HF2-51345.001-A and #HST-HF2-51334.001-A, respectively, awarded by the Space Telescope Science Institute, which is operated by the Association of Universities for Research in Astronomy, Incorporated under NASA contract NAS5-26555. J.M. is supported by the People Programme (Marie Curie Actions) of the European Union Seventh Framework Programme (FP7/2007-2013) under REA grant agreement No. 627288. This work is based on data collected at the ESO VLT (prog.ID 186.A-0798), at the NASA *HST*, and at the NASJ Subaru telescope. Based in part on data collected at Subaru Telescope and obtained from the SMOKA, which is operated by the Astronomy Data Center, NAOJ (Baba et al. 2002).

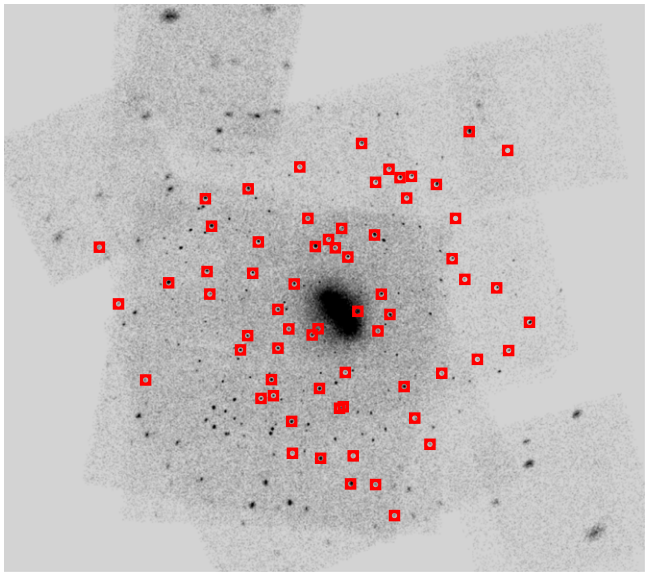

Figure 18. *Chandra* 0.5–7 keV image with overlaid X-ray sources and serendipitously discovered AGNs with spectroscopic redshift from our CLASH-VLT survey. The *Chandra* image shown here is not exposure corrected and not background subtracted, to best show the detected point sources. Note that only a handful of the sources in our spectroscopic catalog are cluster members, while most are foreground and background sources (see Table 8).

APPENDIX A
DETERMINATION OF THE X-RAY MASS PROFILE

The X-ray mass profile has been obtained under the assumption of a spherically symmetric ICM in hydrostatic equilibrium with the underlying gravitational potential. None of the substructures identified in the optical analysis have been masked. We treated the whole X-ray emission, including the secondary X-ray peak of surface brightness, as originating from hot gas in hydrostatic equilibrium in a single dark matter halo. *Chandra* observations (obsID: 16236, 16237, 16304, 16523, 17313; total exposure time: 293 ks) have been reduced and analyzed using CIAO 4.7 and CALDB 4.6.9 to recover a gas density profile from the deprojection of the cumulative surface brightness profile and a gas temperature profile with a local background. The top panel of Figure 16 shows the electron density profiles obtained from both the geometrically

Table 9
Redshifts of Radio Sources in the Field of MACS0416

ID	R.A.	decl.	z	QF	Ref.	Mag
(1)	(2)	(3)	(4)	(5)	(6)	(7)
CLASHVLTJ041705.4-241006	64.272324	−24.168458	0.2700	3	1	18.55
CLASHVLTJ041703.8-241121	64.266004	−24.189252	0.3027	3	1	18.94
CLASHVLTJ041703.5-240603	64.264658	−24.101109	0.5659	3	1	21.48
CLASHVLTJ041653.0-235435	64.220664	−23.909770	0.3983	3	1	19.63
CLASHVLTJ041652.0-235850	64.216827	−23.980742	0.4005	2	1	22.95
CLASHVLTJ041651.7-240546	64.215239	−24.096121	0.2052	3	1	19.89
CLASHVLTJ041648.8-240243	64.203525	−24.045421	1.1785	3	1	21.93
CLASHVLTJ041648.4-240034	64.201492	−24.009517	0.4125	3	1	20.21
CLASHVLTJ041647.7-235706	64.198886	−23.951909	0.3835	3	1	19.74
CLASHVLTJ041647.0-235307	64.195996	−23.885462	0.2994	3	2	19.87

Note. The entire table is available as supplementary material in the Astrophysical Journal Supplement Series, on CDS, and at following URL: https://sites.google.com/site/vltclashpublic/. The full table contains 7 columns and 105 redshifts. Columns list the following information: (1) VIMOS identification number, (2–3) coordinates, (4) spectroscopic redshift, (5) redshift quality flag, (6) reference (i.e., CLASH-VLT VIMOS: 1—based on LR-Blue spectra, 2—based on MR spectra, 3—based on a combination of LR-Blue and MR spectra, 4—Ebeling et al. (2014), 5—*Magellan* (D. Kelson 2016, private communication)), and (7) Subaru R-band magnitude.

(This table is available in its entirety in machine-readable form.)

deprojected surface brightness profile and the normalization of the thermal component (APEC model in Xspec 12.9; Arnaud 1996) fitted to the extracted spectra. The gas temperature has been obtained by spectral fitting with an APEC model in Xspec 12.9. The bottom panel of Figure 16 shows the best-fit 3D temperature profile obtained by inverting the hydrostatic equilibrium equation in combination with the deprojected surface brightness profile. A functional form (the King approximation to the isothermal sphere in the case discussed here; see e.g., Ettori et al. 2002) for the gravitational potential has been assumed and constrained in its two free parameters (normalization and scale radius) by using the observed gas density profile and the hydrostatic equilibrium equation to match the spectroscopic temperature profile (i.e., we apply the backward method described in Ettori et al. (2013). In the mass profile reconstruction presented in Figure 13, at each radius, the errors on the mass profile represent the range of values allowed from the 1σ statistical uncertainties on the two free parameters (i.e., $\Delta\chi^2 = 2.3$). More details on the method used here for the mass reconstruction are presented in Ettori et al. (2010).

APPENDIX B
COMBINED SL AND WL MASS RECONSTRUCTION

We analyzed a lensing mass reconstruction covering the full cluster field and, in particular, the area of interest around the SW substructure. We used a multi-scale grid lensing analysis that combines WL and SL reconstruction following the methodology of Merten et al. (2009). This is the same method used in the analysis of the X-ray relaxed CLASH sample presented in Merten et al. (2015). This lens model of MACS0416 was submitted in the context of the pre-Frontier Fields lens models provided by STScI (http://www.stsci.edu/hst/campaigns/frontier-fields/Lensing-Models) and uses CLASH Subaru/Suprime-Cam WL catalogs (Umetsu et al. 2014), *HST* ACS weak-lensing catalogs (Merten et al. 2015; Zitrin et al. 2015), and the CLASH SL identifications presented in Zitrin et al. (2015). As shown in Figure 17, the surface-mass–density contours, which are derived from 1000 bootstrap realizations of this model, reveal no significant overdensity around the position of the SW concentration of member galaxies. In order to test the robustness of this result which, in this area of the field, is mainly driven by the *HST*/ACS weak-lensing catalog, we performed two checks. First, we used our comprehensive spectroscopic redshift catalog to validate the weak-lensing background selection for the ACS catalog. We find no contamination by foreground objects in the area of interest, which confirms our initial selection based on the CLASH 16-band photometric redshifts. We also performed a reconstruction which is based on an ACS catalog which has no background selection applied at all, but was just cleaned from stars and artefacts. We do this to increase the number of galaxies in the weak-lensing analysis. Although this selection may introduce a dilution of the lensing signal, it ensures that no existing substructure is missed due to insufficient spatial resolution. However, the reconstruction based on this extreme case also shows no significant overdensity in the reconstructed surface-mass density map.

APPENDIX C
REDSHIFTS OF X-RAY SOURCES IN THE FIELD

In our CLASH-VLT survey, we have systematically targeted all the *Chandra* X-ray sources detected in the field of each cluster. In the field of MACS0416, we have obtained redshifts and spectra of 60 *Chandra* sources, plus 5 serendipitously discovered AGNs. Table 8 lists coordinates, magnitudes, and redshifts of these objects. Figure 18 shows the position of all the sources with spectroscopic redshift in the *Chandra* field.

APPENDIX D
REDSHIFTS OF RADIO SOURCES IN THE FIELD

We cross-matched our CLASH-VLT spectroscopic catalog with the catalog of JVLA detected sources in the field of MACS0416. Allowing for a position uncertainty of 3″, we found redshifts and spectra of 105 JVLA sources. Table 9 lists coordinates, magnitudes, and redshifts of these objects.

REFERENCES

Annunziatella, M., Biviano, A., Mercurio, A., et al. 2014, A&A, 571, A80
Annunziatella, M., Mercurio, A., Biviano, A., et al. 2016, A&A, 585, A160
Arnaud, K. A. 1996, in ASP Conf. Ser. 101, Astronomical Data Analysis Software and Systems V, ed. G. H. Jacoby, & J. Barnes (San Francisco, CA: ASP), 17
Ashman, K. M., Bird, C. M., & Zepf, S. E. 1994, AJ, 108, 2348
Baba, H., Yasuda, N., Ichikawa, S.-I., et al. 2002, in ASP Conf. Ser. 281, Astronomical Data Analysis Software and Systems XI, ed. D. A. Bohlender, D. Durand, & T. H. Handley (San Francisco, CA: ASP), 298
Baes, M., & Dejonghe, H. 2002, A&A, 393, 485
Balestra, I., Mainieri, V., Popesso, P., et al. 2010, A&A, 512, A12
Balestra, I., Vanzella, E., Rosati, P., et al. 2013, A&A, 559, L9
Beers, T. C., Flynn, K., & Gebhardt, K. 1990, AJ, 100, 32
Biviano, A., Durret, F., Gerbal, D., et al. 1996, A&A, 311, 95
Biviano, A., Katgert, P., Thomas, T., & Adami, C. 2002, A&A, 387, 8
Biviano, A., Murante, G., Borgani, S., et al. 2006, A&A, 456, 23
Biviano, A., Rosati, P., Balestra, I., et al. 2013, A&A, 558, A1
Bradley, L. D., Zitrin, A., Coe, D., et al. 2014, ApJ, 792, 76
Broadhurst, T., Benítez, N., Coe, D., et al. 2005a, ApJ, 621, 53
Broadhurst, T., Takada, M., Umetsu, K., et al. 2005b, ApJL, 619, L143
Burkert, A. 1995, ApJL, 447, L25
Carter, D., & Metcalfe, N. 1980, MNRAS, 191, 325
Danese, L., de Zotti, G., & di Tullio, G. 1980, A&A, 82, 322
Diaferio, A. 1999, MNRAS, 309, 610
Diaferio, A., & Geller, M. J. 1997, ApJ, 481, 633
Diego, J. M., Broadhurst, T., Molnar, S. M., Lam, D., & Lim, J. 2015, MNRAS, 447, 3130
Donahue, M., Voit, G. M., Mahdavi, A., et al. 2014, ApJ, 794, 136
Dressler, A. 1984, ARA&A, 22, 185
Dressler, A., & Shectman, S. A. 1988, AJ, 95, 985
Ebeling, H., Edge, A. C., & Henry, J. P. 2001, ApJ, 553, 668
Ebeling, H., Ma, C.-J., & Barrett, E. 2014, ApJS, 211, 21
Einasto, J. 1965, TrAlm, 5, 87
Ettori, S., De Grandi, S., & Molendi, S. 2002, A&A, 391, 841
Ettori, S., Donnarumma, A., Pointecouteau, E., et al. 2013, SSRv, 177, 119
Ettori, S., Gastaldello, F., Leccardi, A., et al. 2010, A&A, 524, A68
Fadda, D., Girardi, M., Giuricin, G., Mardirossian, F., & Mezzetti, M. 1996, ApJ, 473, 670
Feretti, L., Giovannini, G., Govoni, F., & Murgia, M. 2012, A&ARv, 20, 54
Ferrari, C., Maurogordato, S., Cappi, A., & Benoist, C. 2003, A&A, 399, 813
Garilli, B., Fumana, M., Franzetti, P., et al. 2010, PASP, 122, 827
Gebhardt, K., & Beers, T. C. 1991, ApJ, 383, 72
Geller, M. J., Diaferio, A., & Kurtz, M. J. 1999, ApJL, 517, L23
Geller, M. J., Diaferio, A., Rines, K. J., & Serra, A. L. 2013, ApJ, 764, 58
Giacintucci, S., Markevitch, M., Venturi, T., et al. 2014, ApJ, 781, 9
Gifford, D., Miller, C., & Kern, N. 2013, ApJ, 773, 116
Girardi, M., Aguerri, J. A. L., De Grandi, S., et al. 2014, A&A, 565, A115
Girardi, M., Barrena, R., Boschin, W., & Ellingson, E. 2008, A&A, 491, 379
Girardi, M., Boschin, W., & Barrena, R. 2010, A&A, 517, A65
Girardi, M., Escalera, E., Fadda, D., et al. 1997, ApJ, 482, 41
Girardi, M., Fadda, D., Giuricin, G., et al. 1996, ApJ, 457, 61
Girardi, M., Mercurio, A., Balestra, I., et al. 2015, A&A, 579, A4
Grillo, C., Suyu, S. H., Rosati, P., et al. 2015, ApJ, 800, 38
Harvey, D., Massey, R., Kitching, T., Taylor, A., & Tittley, E. 2015, Sci, 347, 1462
Hernquist, L. 1990, ApJ, 356, 359
Jauzac, M., Jullo, E., Eckert, D., et al. 2015, MNRAS, 446, 4132
Katgert, P., Biviano, A., & Mazure, A. 2004, ApJ, 600, 657
Koekemoer, A. M., Avila, R. J., Hammer, D., et al. 2014, BAAS, 223, 254.02
Koekemoer, A. M., Faber, S. M., Ferguson, H. C., et al. 2011, ApJS, 197, 36
Kravtsov, A. V., & Borgani, S. 2012, ARA&A, 50, 353
Le Fèvre, O., Saisse, M., Mancini, D., et al. 2003, Proc. SPIE, 4841, 1670
Lemze, D., Postman, M., Genel, S., et al. 2013, ApJ, 776, 91
Lotz, J., Mountain, M., Grogin, N. A., et al. 2014, BAAS, 223, 254.01
Maier, C., Kuchner, U., Ziegler, B. L., et al. 2016, arXiv:1602.00686
Mamon, G. A., Biviano, A., & Boué, G. 2013, MNRAS, 429, 3079
Mann, A. W., & Ebeling, H. 2012, MNRAS, 420, 2120
Markevitch, M., Gonzalez, A. H., Clowe, D., et al. 2004, ApJ, 606, 819
Meneghetti, M., Rasia, E., Vega, J., et al. 2014, ApJ, 797, 34
Merten, J., Cacciato, M., Meneghetti, M., Mignone, C., & Bartelmann, M. 2009, A&A, 500, 681
Merten, J., Meneghetti, M., Postman, M., et al. 2015, ApJ, 806, 4
Meyer, S. L. 1975, Data analysis for scientists and engineers (New York: Wiley)
Munari, E., Biviano, A., Borgani, S., Murante, G., & Fabjan, D. 2013, MNRAS, 430, 2638
Navarro, J. F., Frenk, C. S., & White, S. D. M. 1996, ApJ, 462, 563
Navarro, J. F., Frenk, C. S., & White, S. D. M. 1997, ApJ, 490, 493
Neumann, D. M., Lumb, D. H., Pratt, G. W., & Briel, U. G. 2003, A&A, 400, 811
Newman, A. B., Treu, T., Ellis, R. S., et al. 2009, ApJ, 706, 1078
Newman, A. B., Treu, T., Ellis, R. S., & Sand, D. J. 2011, ApJL, 728, L39
Newman, A. B., Treu, T., Ellis, R. S., & Sand, D. J. 2013, ApJ, 765, 25
Ogrean, G. A., van Weeren, R. J., Jones, C., et al. 2015, ApJ, 812, 153
Patel, B., McCully, C., Jha, S. W., et al. 2014, ApJ, 786, 9
Pisani, A. 1993, MNRAS, 265, 706
Pisani, A. 1996, MNRAS, 278, 697
Plionis, M., & Basilakos, S. 2002, MNRAS, 329, L47
Poole, G. B., Babul, A., McCarthy, I. G., Sanderson, A. J. R., & Fardal, M. A. 2008, MNRAS, 391, 1163
Postman, M., Coe, D., Benítez, N., et al. 2012, ApJS, 199, 25
Powell, M. J. D. 2004, In report DAMTP 2004/NA05, The NEWUOA software for unconstrained optimization without derivatives (Cambridge: Department of Applied Mathematics and Theoretical Physics, Cambridge University)
Rines, K., & Diaferio, A. 2006, AJ, 132, 1275
Rines, K., Geller, M. J., Kurtz, M. J., & Diaferio, A. 2003, AJ, 126, 2152
Rosati, P., Balestra, I., Grillo, C., et al. 2014, Msngr, 158, 48
Sartoris, B., Biviano, A., Rosati, P., et al. 2014, ApJL, 783, L11
Scodeggio, M., Franzetti, P., Garilli, B., et al. 2005, PASP, 117, 1284
Scodeggio, M., Franzetti, P., Garilli, B., Le Fèvre, O., & Guzzo, L. 2009, Msngr, 135, 13
Serra, A. L., Diaferio, A., Murante, G., & Borgani, S. 2011, MNRAS, 412, 800
Silverman, B. W. 1986, Density Estimation for Statistics and Data Analysis (London: Chapman and Hall)
Springel, V., Frenk, C. S., & White, S. D. M. 2006, Natur, 440, 1137
Tiret, O., Combes, F., Angus, G. W., Famaey, B., & Zhao, H. S. 2007, A&A, 476, L1
Umetsu, K., Medezinski, E., Broadhurst, T., et al. 2010, ApJ, 714, 1470
Umetsu, K., Medezinski, E., Nonino, M., et al. 2014, ApJ, 795, 163
Umetsu, K., Zitrin, A., Gruen, D., et al. 2015, arXiv:1507.04385
von der Linden, A., Allen, M. T., Applegate, D. E., et al. 2014, MNRAS, 439, 2
Zitrin, A., Broadhurst, T., Umetsu, K., et al. 2009, MNRAS, 396, 1985
Zitrin, A., Fabris, A., Merten, J., et al. 2015, ApJ, 801, 44
Zitrin, A., Meneghetti, M., Umetsu, K., et al. 2013, ApJL, 762, L30